Journal of Nuclear Materials 393 (2009) 387–408

Contents lists available at ScienceDirect

Journal of Nuclear Materials

journal homepage: www.elsevier.com/locate/jnucmat

In situ studies and modeling the fracture of Zircaloy-4

B.V. Cockeram [a,*], K.S. Chan [b]

[a] Bechtel-Bettis Atomic Power Laboratory, P.O. Box 79, West Mifflin, PA 15122-0079, United States
[b] Southwest Research Institute, San Antonio, TX 78238, United States

ARTICLE INFO

Article history:
Received 24 February 2009
Accepted 19 June 2009

ABSTRACT

In situ fracture studies were performed on non-irradiated Zircaloy-4 using tensile specimens and pre-cracked Compact Tension (CT) specimens to clarify the mechanism for fracture initiation in the constrained and non-constrained state. Similar approaches have been taken in the literature to understand the role of hydrides on the fracture of Zircaloy-4, but hydride-free Zircaloy-4 has received little study. Both annealed and beta-treated Zircaloy-4 were tested in the longitudinal, transverse, and short-transverse orientations to study the role of microstructure and orientation. Unstable crack extension is shown to occur under plastic constraint by a process of void nucleation, growth, and coalescence initiating from the Laves phase particles in the microstructure. A micromechanical model is developed for ductile tearing by void growth and coalescence. Excellent agreement between the model and experiments are observed. Aspects of the fracture mechanism and model are discussed.

1. Introduction

Zircaloy-4 has a hexagonal crystal structure and consists of Zr with Sn, Fe, and Cr in solid solution along with Laves phase intermetallic precipitates that are generally less than about 0.4 μm in diameter [1–4]. The Laves phases are either $Zr(Fe,Cr)_2$, $ZrFe_2$ or $ZrCr_2$ second phase intermetallic precipitates with $Zr(Fe,Cr)_2$ generally the most common [5–7]. The role of texture and these particles on fracture have received some limited study [4,8–19], but the dominant failure mechanism has not been clarified. In situ fracture studies of Zircaloy-4 have been used to show that microcrack formation and coalescence at hydride particles produces the degradation in the fracture toughness of hydrided Zircaloy-4 [8,9]. Ductile crack extension and crack blunting were observed for Zircaloy-4 specimens that did not contain hydrogen [8,9], but the exact mechanism for deformation and crack propagation was not clarified. Post-test fractographic examinations have been used to reveal mechanisms of dimple formation, void coalescence, crack propagation on slip bands, and ridge deformation [4,10–22], but the processes that lead to these features have not been described.

The purpose of this work is to clarify the mechanisms for plasticity and crack extension in wrought Zircaloy-4 using in situ fracture studies in a Scanning Electron Microscope (SEM). Zircaloy-4 specimens are tested in the alpha-annealed and beta-treated conditions [4] to evaluate the role of microstructure on the deformation processes. Pre-cracked Compact Tension (CT) and smooth tapered tensile specimens are machined in three orthogonal orientations to evaluate the role of texture and constraint on the mechanisms for deformation and fracture.

2. Materials and experimental procedure

The nominal composition for the reactor grade Zircaloy-4 used to produce both alpha-annealed and beta-treated material is given in Table 1. Compact-tension (CT) specimens were machined in the LT (longitudinal) and TL (Transverse) orientations (19.8 mm in width, 19.1 mm in height, and 4.8 mm in thickness [23,24]) and SL (through thickness) orientation (16.5 mm in width, 15.9 mm in height, and 3.2 mm in thickness). Tapered tensile specimens were machined in the longitudinal and transverse orientations (28.6 mm long, 2.3 mm thick, and 7.2 mm wide at the ends tapering to a 3.6 mm wide gage section in the center that was 6.4 mm in length) and in the thickness orientation (15.9 mm long, 2.3 mm thick, and 7.2 mm wide at the ends tapering to a 3.6 mm wide gage section in the center that was 3.5 mm in length). After machining, the tensile and CT specimens were mechanically polished to 6 μm finish and etched in a solution of 30% HNO_3, 5% HF, and 65% water for 15 s. The CT specimens were pre-cracked at ambient temperature by compression/compression fatigue using ASTM E812-97 [25] and E813-95 [26] as a guide. The ratio, R, of the minimum load (P_{min}) to the maximum load (P_{max}) in the fatigue cycles was maintained at about 0.1 and a stress range of 61 or 76 MPa was used. The test frequency was 15 Hz and the stress intensity range was 40 MPa $\sqrt{m}$. The stress intensity factor was computed by treating the specimen as a single-edge crack in uniform compression [27].

* Corresponding author.
E-mail address: cockeram@bettis.gov (B.V. Cockeram).

0022-3115/$ - see front matter © 2009 Elsevier B.V. All rights reserved.
doi:10.1016/j.jnucmat.2009.06.033

Table 1
Nominal Chemical Composition of Zircaloy-4 (wt%).

Element	Zr	Sn	Fe	Cr	Ni	Hf	C	O	Si	Al
Composition	Bal	1.51	0.22	0.11	<.0035	.0049	.01	.15	.01	.0057

The number of fatigue cycles ranged from 10,000–42,000 to give crack lengths ranging from 5.8–8.8 mm with a final crack length to specimen width ratio, a/W, between 0.55 to 0.59.

Representative microstructures for the alpha-annealed and beta-treated Zircaloy-4 [4] are shown in Figs. 1 and 2, respectively. Equiaxed grains with a median grain diameter of nominally 25 μm in diameter are observed for the alpha-annealed material, while the typical Widmanstätten or basket-weave microstructure consisting of colonies within prior beta grain boundaries is observed for the beta-treated material. Orientation Imaging Microscopy (OIM) was performed on all tensile and CT specimens prior to testing using a Phillips XL-30 SEM at an accelerating voltage of 20 kV and spot size of 5 at EBSD Analytical (Lehi, Utah) using EDAX/TSL software to collect and analyze the Electron Backscatter Diffraction (EBSD) patterns. Typical results for alpha-annealed and beta-treated materials showing the pole figures, inverse pole figures, grain size distribution, and grain boundary misorientation angle distribution also are provided in Figs. 1 and 2, respectively. The Kearns numbers [28,29], which are a measure of texture based on the volume fraction of basal poles in three reference directions, also were obtained for the individual specimens. Average values for the Kearns numbers, grain size, and misorientation angle are provided in Table 2. As expected, strong texture was observed for the alpha-annealed material with the basal poles oriented predominantly within ±30° of the plate normal, giving rise to a low Kearns number for the longitudinal direction. The grain misorientations exhibited a broad range of misorientation angle. A more random texture is observed for beta-treated Zircaloy-4 with each Widmanstätten lath grain typically having a misorientation angle of 60°. Precipitates rich in Fe and Cr are resolved within higher magnification images, but the Laves phase precipitates were too small in size for a phase identification to be completed using EBSD. The Laves phase precipitates were located at grain boundaries and within grains for alpha-annealed Zircaloy-4, but were primarily located at the lath boundaries for beta-treated Zircaloy-4.

In situ fracture toughness testing was performed in a SEM at SwRI, San Antonio, TX, using a loading stage [30] with the majority of testing performed at room-temperature and a subset performed at 316 °C. Reference micrographs of the near-tip region were taken (250× to 2000× magnification) under a small load (50–150 N) prior to fracture toughness testing. Tensile loads were then applied to the test specimens at K levels in planned increments of 9, 12, 15, 18, 21, 24, 27, 30, 35, 40, 45, and 50 MPa $\sqrt{m}$. The in situ fracture testing was performed under load control where the load was achieved by pulling the specimens to defined displacement values. After applying a set load, the displacement remained constant, and the effective load would decrease slightly as crack advance was observed. The load reduction was recorded and utilized to compute the current stress intensity factor after the crack length was determined subsequently. At a given K level, still photographs of the near-tip region were taken and the corresponding crack extension (Δa), when occurred, was measured directly from the near-tip images. This process was then repeated at a higher K level in intervals of 3–5 MPa $\sqrt{m}$ until the fracture toughness test was terminated when the specimen failed or the maximum travel (displacement) of the loading stage was reached.

In situ tensile testing was performed at ambient temperature. The region of interest in the center of the gauge section of wedge-type tensile specimens was selected and photographed prior to testing. The in situ loading of individual specimens stage was performed to total elongation strains of 5–10% strains before the maximum displacement travel was reached. No voids were observed at these strain levels in any of the tensile specimens tested. Thus, the tensile tests were continued in an MTS testing machine using a conventional test procedure at room-temperature at a displacement rate of 1.3E−2 mm/s, and then SEM examinations were performed.

Post-test SEM fractography was performed on a selected set of specimens. Metallographic sectioning of the deformed specimens was also performed to characterize the fracture mechanism.

3. Results and discussion for in situ fracture studies

3.1. In situ fracture results

The K-resistance curves for alpha-annealed and beta-treated Zircaloy-4 tested at room-temperature are shown in Figs. 3 and 4, respectively. The calculated results shown in these plots are based on a micromechanical model that is presented later in the paper. Limited results for alpha-annealed material tested at 316 °C are shown in Fig. 5. A summary of results for the critical toughness to initiate crack growth (K_c) and K level at steady-state (K_{SS}) are given in Table 3. An initial test of alpha-annealed Zircaloy-4 in the LT orientation performed at 316 °C showed large amounts of crack tip plasticity with extensive crack blunting. Increasing the K to 18 MPa $\sqrt{m}$ resulted in the formation of slip lines, and a limited amount of crack advance occurred very quickly at a K of 21 MPa $\sqrt{m}$ by plastic extension along a slip band, see Fig. 6. Loading the specimen to a K level of about 26 MPa $\sqrt{m}$ resulted in very extensive plastic deformation at the crack tip, as the specimen quickly opened-up by plastic deformation to the point of maximum displacement travel for the loading system with limited crack extension by a ductile process. Closer examination of the specimen revealed that a void was observed near the crack tip, see Fig. 6. The K-resistance curve for LT alpha-annealed material tested at 316 °C in Fig. 5 is an overly-conservative estimate of the fracture toughness for Zircaloy due to the extensive crack tip plasticity. The true fracture toughness measured at temperatures near 316 °C would be much larger (48–60 MPa $\sqrt{m}$ for literature data [4]). A second test of LT alpha-annealed Zircaloy-4 was performed at room-temperature, where the deformation generally was less extensive and occurred more slowly.

For the testing of alpha-annealed Zircaloy-4 at room-temperature shown in Fig. 3, rising R-curve behavior was observed in the L–T and T–L orientations with crack extension starting at K values on the order of 36–40 MPa $\sqrt{m}$ and increasing to values of 58–62 MPa $\sqrt{m}$. Crack extension was observed in the S–L orientation for alpha-annealed starting at a higher K value of 53 MPa $\sqrt{m}$, but a much smaller rise in the K-resistance curve occurred over a short displacement as unstable crack extension occurred at a K of 57 MPa $\sqrt{m}$. The S–L orientation for the highly textured alpha-annealed Zircaloy-4 is in an orientation where it is more difficult to produce slip, so that higher K levels are needed to initiate the deformation processes that result in crack extension. This results in slightly higher K_c values to initiate crack propagation in the S–

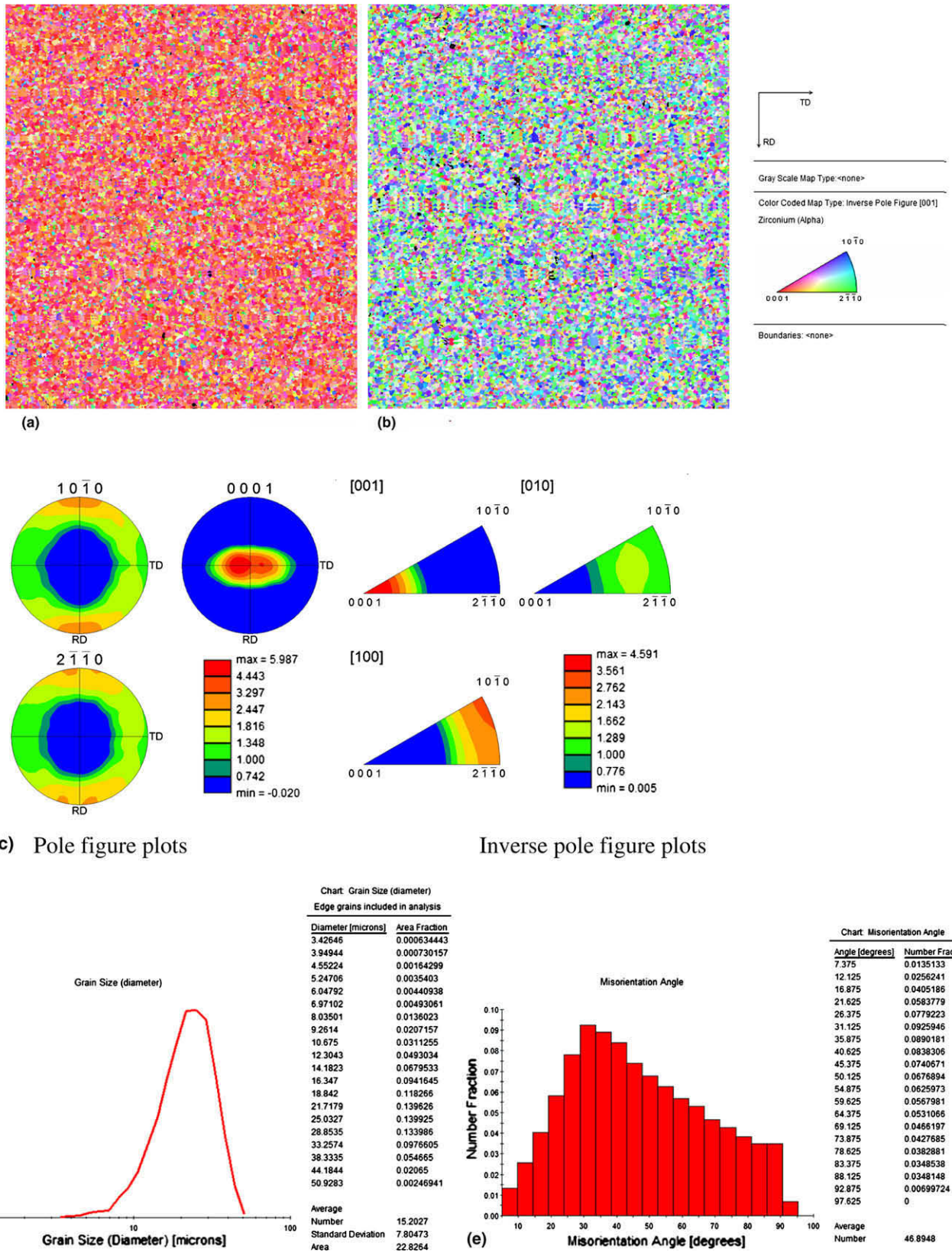

Chart: Grain Size (diameter)
Edge grains included in analysis

Diameter [microns]	Area Fraction
3.42646	0.000634443
3.94944	0.000730157
4.55224	0.00164299
5.24706	0.0035403
6.04792	0.00440938
6.97102	0.00493061
8.03501	0.0136023
9.2614	0.0207157
10.675	0.0311255
12.3043	0.0493034
14.1823	0.0679533
16.347	0.0941645
18.842	0.118266
21.7179	0.139626
25.0327	0.139925
28.8535	0.133986
33.2574	0.0976605
38.3335	0.054665
44.1844	0.02065
50.9283	0.00246941
Average Number	15.2027
Standard Deviation	7.80473
Area	22.8264

Chart: Misorientation Angle

Angle [degrees]	Number Fraction
7.375	0.0135133
12.125	0.0256241
16.875	0.0405186
21.625	0.0583779
26.375	0.0779223
31.125	0.0925946
35.875	0.0890181
40.625	0.0838306
45.375	0.0740671
50.125	0.0676894
54.875	0.0625973
59.625	0.0567981
64.375	0.0531066
69.125	0.0466197
73.875	0.0427685
78.625	0.0382881
83.375	0.0348538
88.125	0.0348148
92.875	0.00699724
97.625	0
Average Number	46.8948

Fig. 1. Example of OIM/EBSD results for alpha-annealed Zircaloy-4 specimens: (a) surface of the CT specimen in the longitudinal (L–T) orientation, (b) surface of the CT specimen in the through thickness (S–L) orientation, (c) pole and inverse pole figure for the Zr-4 CT specimen in the longitudinal (L–T) orientation, (d) OIM measurements of grain size distribution, and (e) OIM measurements of grain boundary misorientation angle distribution.

L orientation in comparison to the L–T and T–L orientations. The tendency for limited plasticity in the S–L orientation results in unstable crack extension at slightly lower K values than the L–T and T–L orientations with no R-curve behavior for the S–L orienta-

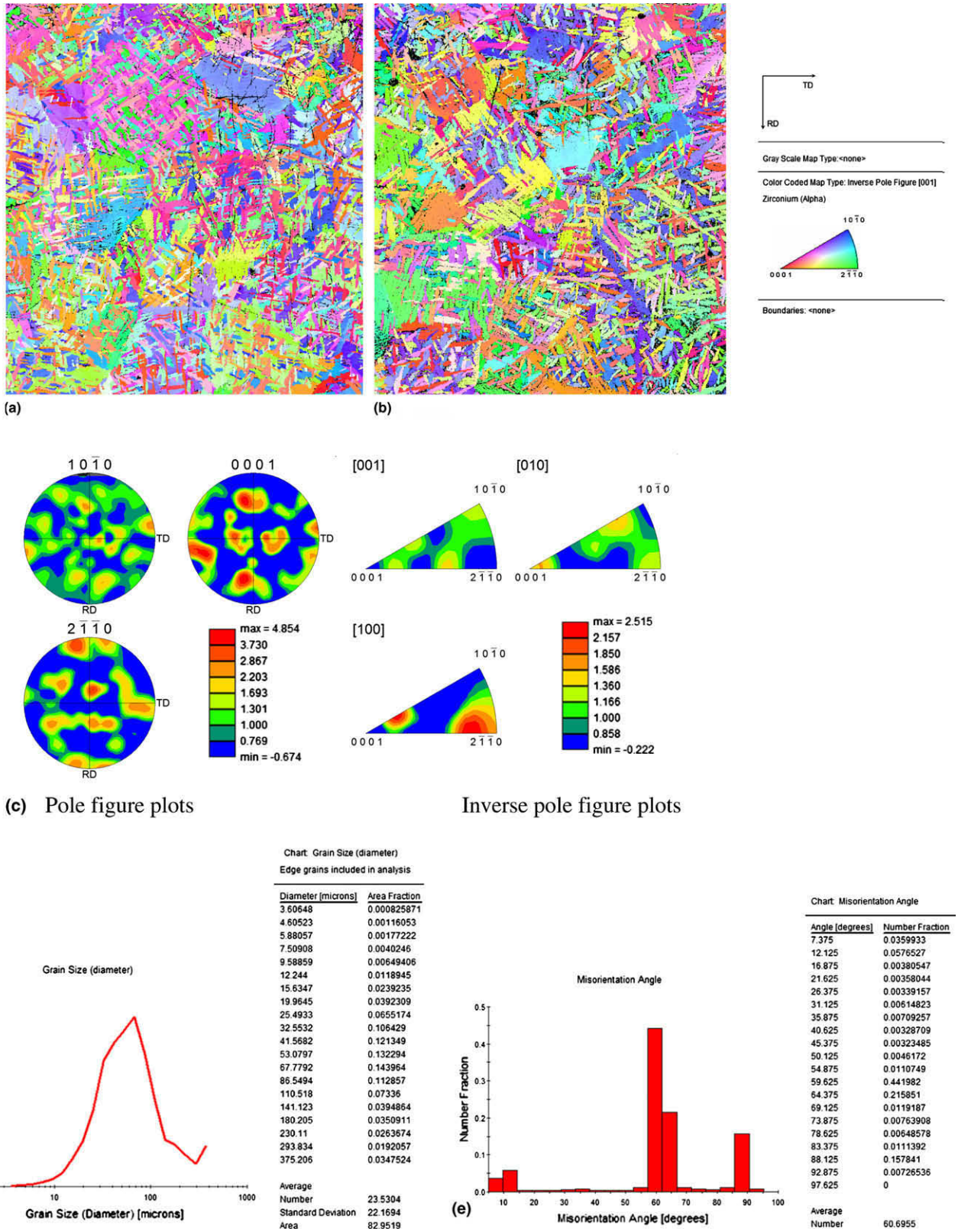

Chart: Grain Size (diameter)
Edge grains included in analysis

Diameter [microns]	Area Fraction
3.60648	0.000825871
4.60523	0.00116053
5.88057	0.00177222
7.50908	0.0040246
9.58859	0.00649406
12.244	0.0118945
15.6347	0.0239235
19.9645	0.0392309
25.4933	0.0655174
32.5532	0.106429
41.5682	0.121349
53.0797	0.132294
67.7792	0.143964
86.5494	0.112857
110.518	0.07336
141.123	0.0394864
180.205	0.0350911
230.11	0.0263674
293.834	0.0192057
375.206	0.0347524
Average	
Number	23.5304
Standard Deviation	22.1694
Area	82.9519

Chart: Misorientation Angle

Angle [degrees]	Number Fraction
7.375	0.0359933
12.125	0.0576527
16.875	0.00380547
21.625	0.00358044
26.375	0.00339157
31.125	0.00614823
35.875	0.00709257
40.625	0.00328709
45.375	0.00323485
50.125	0.0046172
54.875	0.0110749
59.625	0.441982
64.375	0.215851
69.125	0.0119187
73.875	0.00763908
78.625	0.00648578
83.375	0.0111392
88.125	0.157841
92.875	0.00726536
97.625	0
Average	
Number	60.6955

Fig. 2. Example of OIM/EBSD results for beta-treated Zircaloy-4 specimens: (a) surface of CT specimen in the longitudinal (L–T) orientation, (b) surface of the CT specimen in the through thickness (S–L) orientation, (c) pole and inverse pole figure for the CT specimen in the longitudinal (L–T) orientation, (d) OIM measurements of grain size distribution, and (e) OIM measurements of grain boundary misorientation angle distribution.

tion. A similar trend in results was observed for the testing at 316 °C in Fig. 5, but the tendency for plasticity and *R*-curve behavior was much greater. For the testing at 316 °C, crack initiation occurred in the S–L orientation at a slightly higher *K*, but the

Table 2
Summary of the OIM results of the Kearns parameter, the grain size, and the mean value of the grain boundary misorientation angle for individual specimens.

Heat treatment	Average Kearns parameter/range of values			Grain size mean/standard deviation (μm)	Average grain boundary misorientation angle (°)
	Normal	Longitudinal	Transverse		
Alpha-annealed	0.675/0.622–0.710	0.080/0.069–0.088	0.243/0.209–0.307	15.2/7.8	47.6
Beta-treated	0.390/0.341–0.423	0.291/0.255–0.329	0.320/0.300–0.331	23.6/23.7	61.1

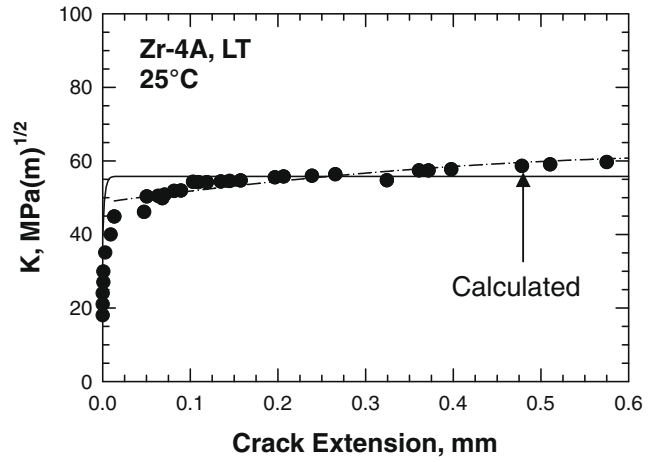

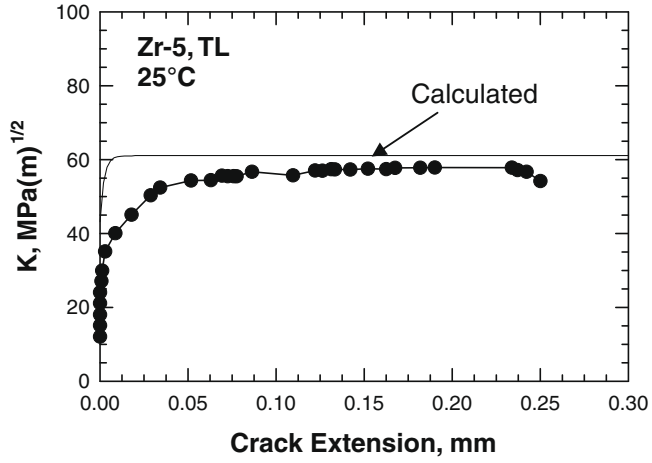

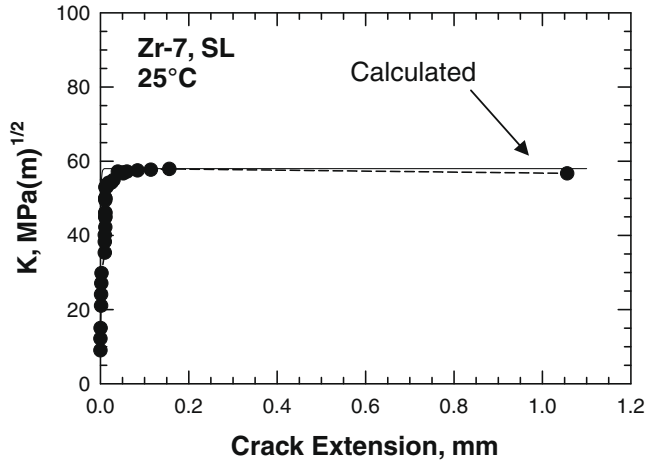

Fig. 3. Comparison of computed and measured *K*-resistance curves for the alpha-annealed Zircaloy-4 CT specimens tested at room-temperature (25 °C). The calculated lines are the solid lines indicated above, while the measures values are the lines connecting the data points.

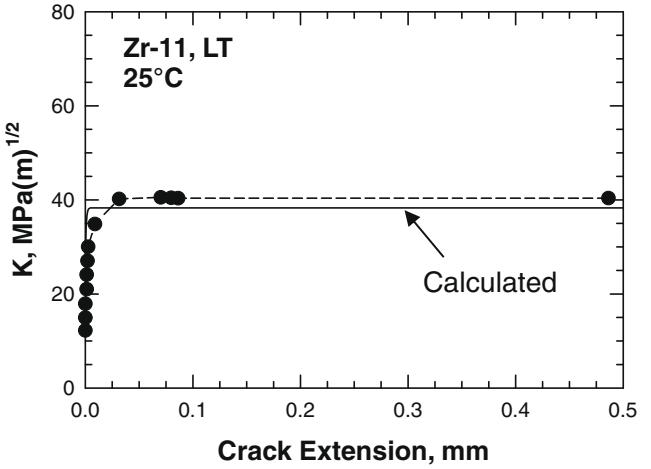

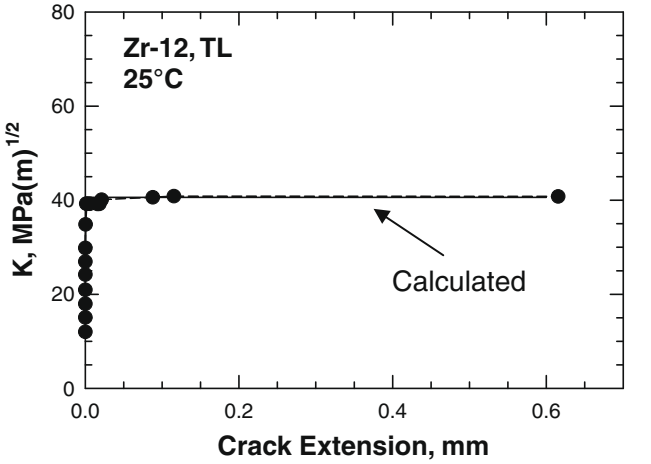

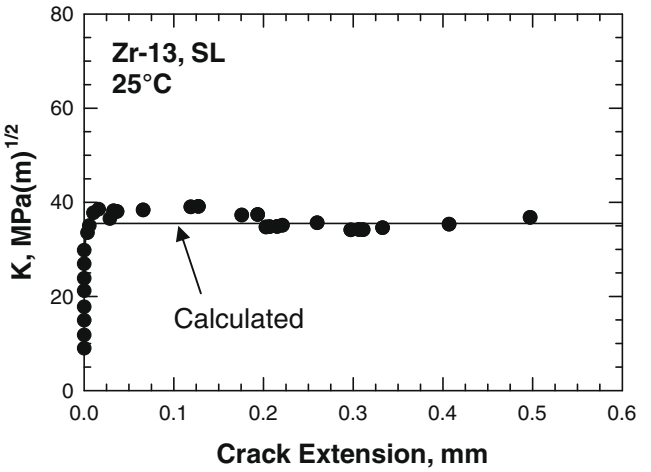

Fig. 4. Comparison of computed and measured *K*-resistance curves for the beta-treated Zircaloy-4 CT specimens tested at room-temperature (25 °C). The calculated lines are the solid lines indicated above, while the measures values are the lines connecting the data points.

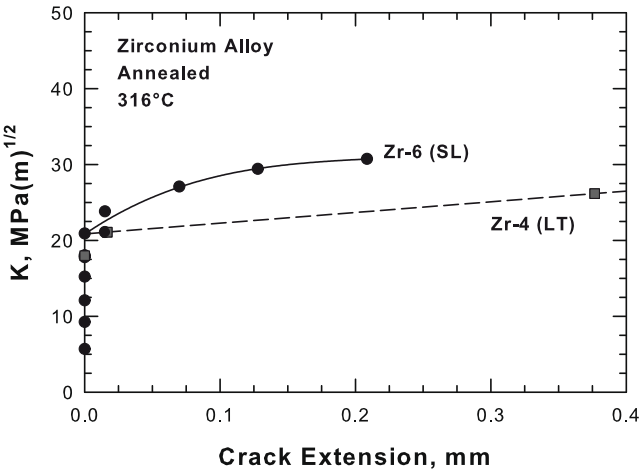

Fig. 5. *K*-resistance curves for alpha-annealed Zircaloy-4 CT specimens tested at 316 °C.

K-resistance curve increased to saturation at much lower displacements than observed for the L–T orientation. For the L–T orientation tested at 316 °C, a rising *K*-resistance curve would likely be observed if greater displacement travel could be achieved with the in situ test system.

The *K*-resistance curves for beta-treated Zircaloy-4 tested at room-temperature show in Fig. 4 the crack extension started at values between 35–39 MPa $\sqrt{m}$ for all orientations, and the crack extension was generally unstable with no rising *R*-curve behavior observed with crack extension. The only exception was the rise of K = 35 MPa $\sqrt{m}$ to K = 40 MPa $\sqrt{m}$ over a very small crack extension of 0.023 mm observed for L–T beta-treated Zircaloy-4, but further extension was shown to be unstable at K = 40 MPa $\sqrt{m}$. The K levels at which crack initiation is observed (35–40 MPa $\sqrt{m}$) and maximum K at steady state crack extension (39–41 MPa $\sqrt{m}$) are shown in Table 3 to be comparable for the L–T, T–L, and S–L orientations, indicating the fracture toughness values are isotropic. This is consistent with the more random texture observed for beta-treated Zircaloy-4.

The K values for crack initiation at room-temperature for beta-treated material (K_c = 35–39 MPa $\sqrt{m}$) are at the lower range of values for alpha-annealed Zircaloy-4 (35–53 MPa $\sqrt{m}$). The K_c values determined in this work are consistent with fracture toughness values reported in the literature [4,8–10,19–22,31,32]. Rising *R*-curve behavior was observed for alpha-annealed Zircaloy-4 in the L–T and T–L orientations, while unstable crack extension to failure with a flat *K*-resistance curve was observed for the S–L alpha-annealed specimen and all beta-treated specimens. The rise in K to the steady state value for crack propagation occurs at higher values for the alpha-annealed (K_{SS} = 57–52 MPa $\sqrt{m}$) than for

Table 3
Summary of the test temperature (T), yield stress (σ_y), ultimate tensile strength (σ_{UTS}), the stress intensity factors at the onset of crack growth (K_c) and at steady-state (K_{SS}) of the *K*-resistance curve for individual compact-tension specimens.

Specimen	Heat treatment	Orientation	T,C	σ_y (MPa)	σ_{UTS} (MPa)	K_c (MPa) $\sqrt{m}$	K_{SS} (MPa) $\sqrt{m}$
Zr-4A	Alpha-annealed	LT	25	365.3	506.7	48.7	62.2
Zr-4		LT	316	–	–	19.5	–
Zr-5		TL	25	354.9	513.1	35.1	60.2
Zr-7		SL	25	362.8	602.3	53	57.4
Zr-6		SL	316	–	–	23.8	30.7
Zr-11	Beta-treated	LT	25	327.3	552.8	34.9	40.4
Zr-12		TL	25	327.9	553.6	39.2	40.6
Zr-13		SL	25	354.4	556.6	37.8	38.6

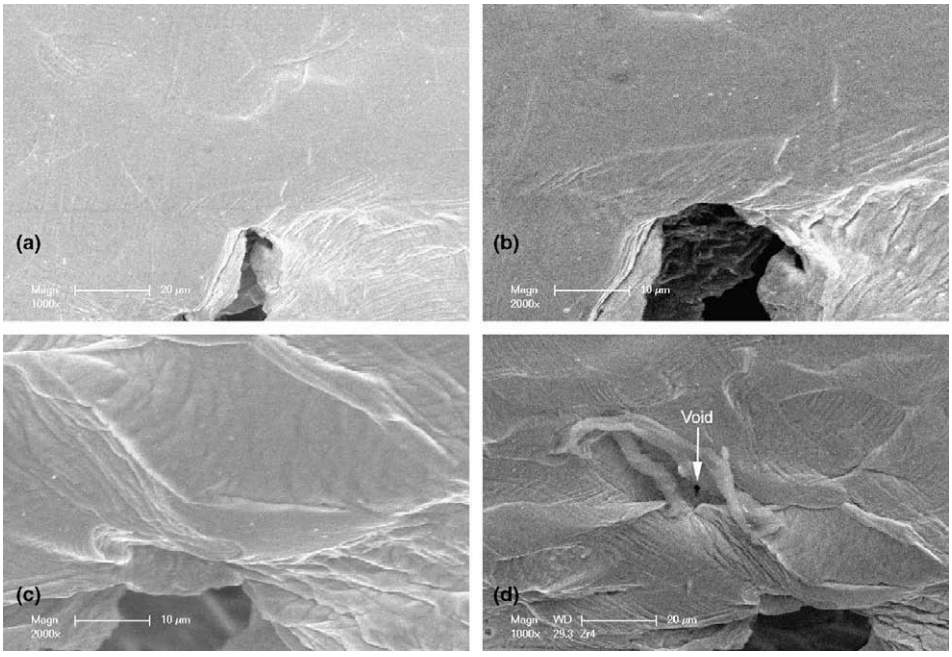

Fig. 6. Processes for crack extension observed for an alpha-annealed Zircaloy-4 CT specimen in the LT orientation (Zr-4) tested at 316 °C: (a) crack tip at 18 MPa $\sqrt{m}$, (b) crack tip at 21 MPa $\sqrt{m}$, (c) crack tip at 24 MPa $\sqrt{m}$, and (d) crack at 24 MPa $\sqrt{m}$ showing a void formed at the crack tip.

beta-treated (K_{SS} = 39–40 MPa $\sqrt{m}$). Detailed examinations of crack extension are presented in the following sections to understand these differences in fracture resistance between alpha-annealed and beta-treated Zircaloy-4.

3.2. Examinations of alpha-annealed Zircaloy-4

Crack propagation at lower K values of 35–40 MPa $\sqrt{m}$ in L–T alpha-annealed Zircaloy-4 was observed to occur by shearing along slip lines, see Fig. 7a and b. Void formation and coalescence was observed to produce crack propagation in Fig. 7 at higher K values of 50–53 MPa $\sqrt{m}$. A similar process of crack propagation along slip lines was observed for T–L alpha-annealed at lower K values of 35–55 MPa $\sqrt{m}$ in Fig. 8a–d. Crack propagation by void formation and coalescence was observed to occur for T–L at a higher K of 60 MPa $\sqrt{m}$ in Fig. 8. For the S–L orientation, a small amount of crack extension occurred along a slip line at K = 30–35 MPa $\sqrt{m}$, but the crack did not extend at higher K levels, see Fig. 9. Instead, loading the S–L specimen to K = 45 MPa $\sqrt{m}$ resulted in the formation of a void along a shear band behind the crack. Loading to yet higher applied K resulted in void coalescence along the shear band to produce crack extension. Additional crack extension in the S–L orientation occurred by the emission of slip lines from the crack tip and subsequent decohesion along the slip lines without voids being observed at the surface. The mechanism for crack propagation at 316 °C appeared to be the same as observed at room-temperature. Fig. 6 shows crack extension occurred for alpha-annealed in the L–T orientation along slip lines, and void formation was observed at the crack tip. Crack extension along slip lines is also observed for the S–L orientation tested at 316 °C in Fig. 10. SEM examinations on the inside of the crack surface show in Fig. 10e and f that although voids may not be observed at the surface, void formation and coalescence occurs along the crack plane below the surface.

Metallographic evidence for void formation and coalescence in the interior of the specimens within the crack tip plastic zone were determined by sectioning the CT specimens at the mid-thickness. Fig. 11 shows that a number of voids were observed directly ahead of the crack tip for the L–T, T–L, and S–L orientations. The voids observed for the L–T orientation appear to be in the process of linking up with the crack tip in Fig. 11a, and removing surface material by

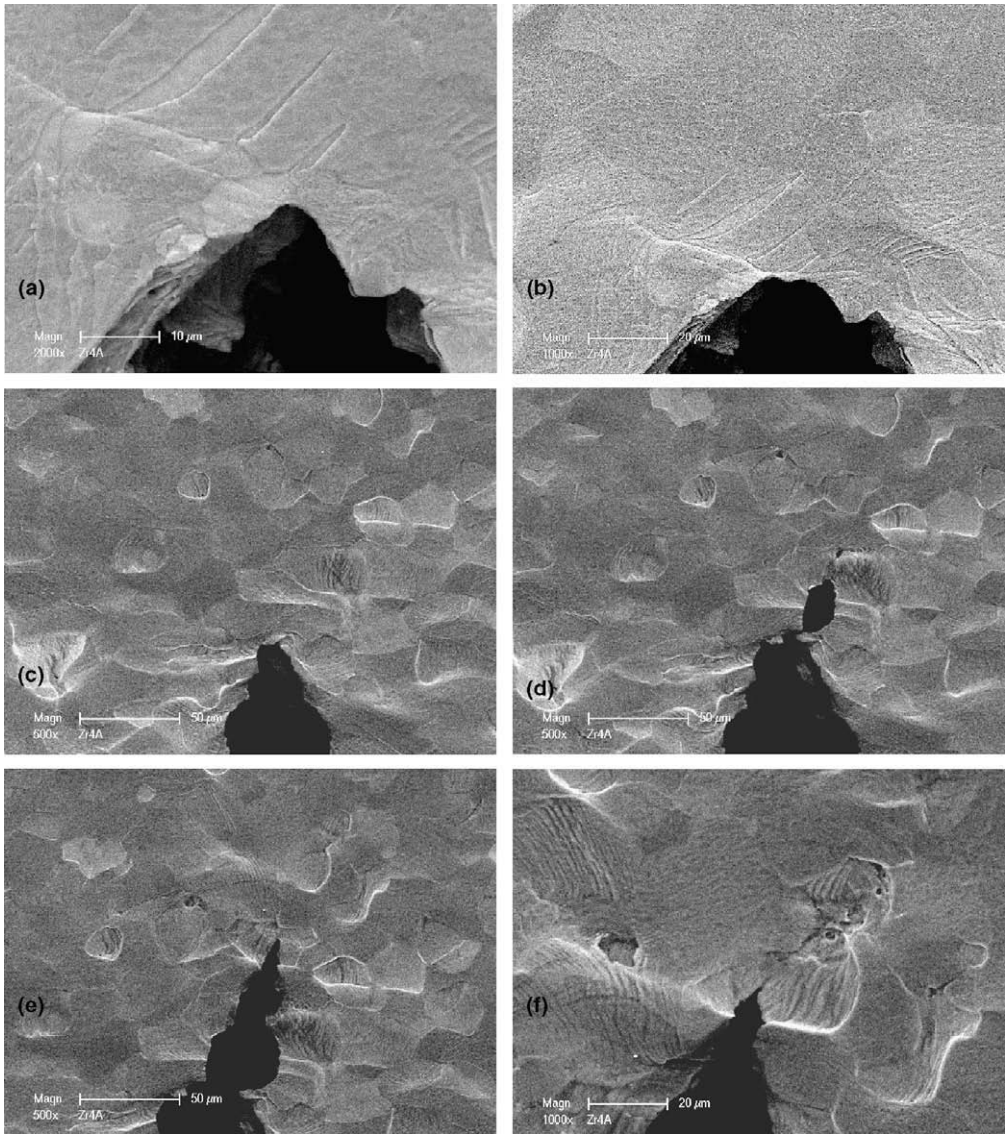

Fig. 7. Processes for crack extension observed for an alpha-annealed Zircaloy-4 CT specimen in the LT orientation (Zr-4a) tested at room-temperature: (a) local slip along lines at 35 MPa $\sqrt{m}$, (b) crack extension along lines at 40 MPa $\sqrt{m}$, (c) blunt crack tip at 53 MPa $\sqrt{m}$, (d) void formation and linking with the blunt crack tip at 53 MPa $\sqrt{m}$, (e) crack tip with the coalesced voids at 53 MPa $\sqrt{m}$, and (f) void formation ahead of the sharpened tip at 53 MPa $\sqrt{m}$.

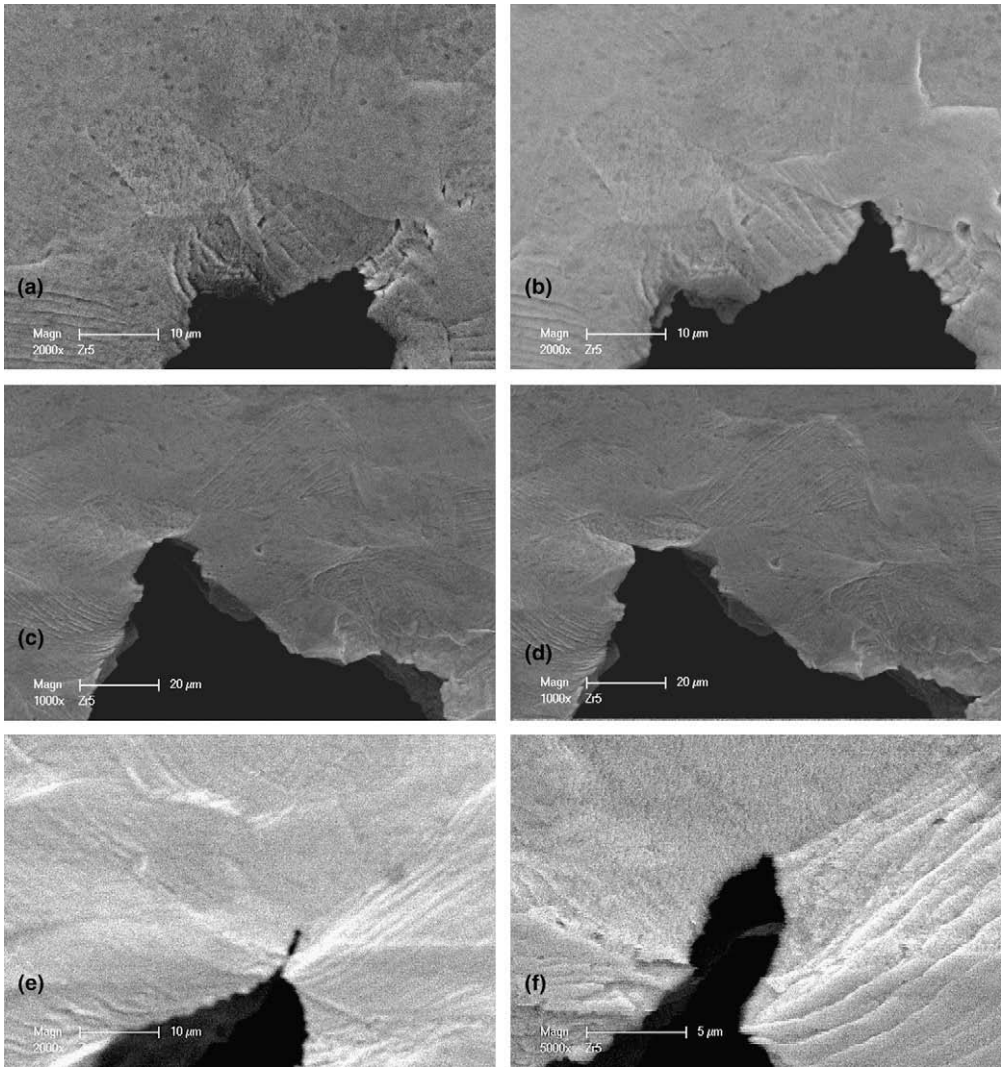

Fig. 8. Processes for crack extension observed for an alpha-annealed Zircaloy-4 CT specimen in the TL orientation (Zr-5) tested at room-temperature: (a) local slip along lines at 40 MPa $\sqrt{m}$, (b) crack extension along a slip line at 45 MPa $\sqrt{m}$, (c) slip line emission from crack tip at 55 MPa $\sqrt{m}$, (d) slip line fracture into V-shaped sharp crack at 55 MPa $\sqrt{m}$, (e) void expanding and linking with crack tip at 60 MPa $\sqrt{m}$, and (f) rounded blunt crack tip from void expansion at 60 MPa $\sqrt{m}$.

additional polishing shows in Fig. 11b that the largest voids had indeed linked up with the crack tip. These metallographic examinations indicate the same processes of void nucleation, growth, and coalescence observed during the in situ tests at the polished surface of the specimen were also occurring within the bulk of the specimens. Fractography of T–L and S–L specimens shows in Fig. 12 that numerous voids, dimples, tearing ridges, and markings of wavy slip are present at the fracture surface. Higher magnification images of the tearing ridges show that voids nucleated from tiny Laves phase particles on the fracture surface. A key observation from the fracture surface is that void and tearing ridge features were observed across the fracture surface regardless of their location with respect to the initial crack tip. This indicates void formation may occur along slip bands at any point in the fracture process.

Based on the in situ examinations of crack extension, metallography, and fractography examinations, the crack extension in alpha-annealed Zircaloy-4 results from the formation of voids along slip bands due to slip band intersections with grain boundaries, Laves phase particles, or other slip bands. Void coalescence along the slip bands results in crack extension. This is a ductile mode for crack extension, as void coalescence occurs by the plastic stretching and elongation of the remaining metal ligaments between the voids. The initial stage of crack extension along slip bands observed for L–T and T–L at lower K values corresponds to the rising part of the K-resistance curves, while the formation of voids was observed to occur at K levels where unstable crack extension began to occur. For S–L Zircaloy-4, crack extension began as an unstable process with void formation observed at the surface along a slip band. In all cases where crack extension occurred along a slip band, void formation may occur along the slip plane below the surface, but such a process cannot be confirmed by these surface examinations. These examinations suggest void formation and coalescence is a key deformation process that leads to unstable crack extension or plastic instability. The rising part of the K-resistance curves observed for the alpha-annealed LT and TL specimens likely results from small-scale crack extension along slip bands without void formation and coalescence, while void formation and coalescence results in an unstable mode of crack extension signified by the flat part of the K-resistance curve.

3.3. Examinations of beta-treated Zircaloy-4

The K-resistance curves for beta-treated Zircaloy-4 were shown in Fig. 4 to consist of unstable crack extension at similar K values for the LT, TL, and SL orientations. Crack blunting with no visible

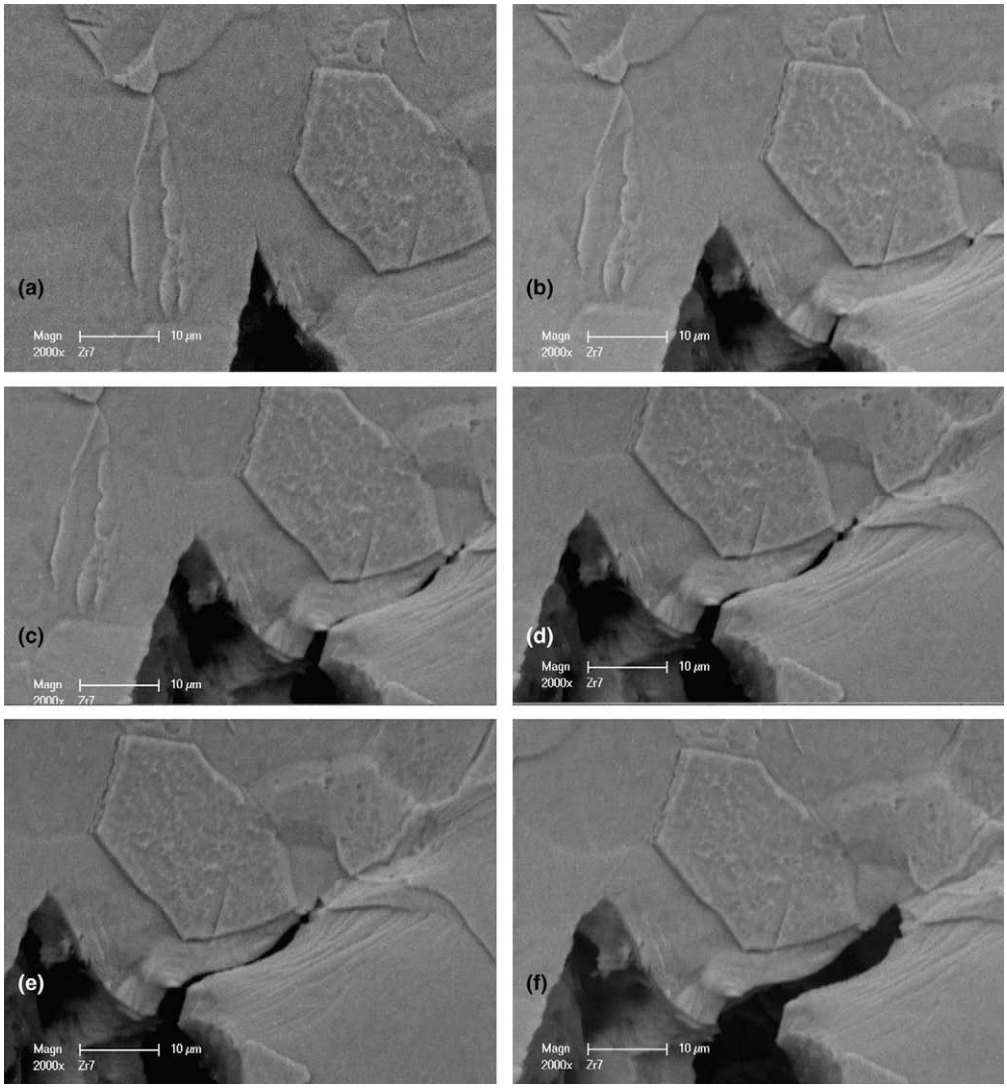

Fig. 9. Processes for crack extension observed for an alpha-annealed Zircaloy-4 CT specimen in the SL orientation (Zr-7) tested at room-temperature during loading from 35 to 45 MPa $\sqrt{m}$: (a) local shear developed behind the main crack tip, (b) partial decohesion and void formation along the slip band, (c) slip band decohesion to form voids and microcracks, (d) linkage of voids and microcracks to completely separate the slip band into a crack, (e) and (f) additional opening of the newly formed crack.

slip line formation ahead of the crack tip was observed in Fig. 13a for the LT orientation at K values between 15 and 35 MPa $\sqrt{m}$. Shearbands and voids were observed in Fig. 13b and c to form along the boundaries between the lath grains, and crack propagation was observed to occur by coalescence of these voids along the lath boundaries. This main crack was observed to propagate to failure in an unstable manner at K = 40 MPa $\sqrt{m}$ for the LT orientation. A similar fracture process was shown for the TL orientation in Fig. 14 where crack tip blunting with no crack extension was again observed at K values between 15 and 36 MPa $\sqrt{m}$. Loading the TL specimen at finer K increments allowed the intensification of a slip line (labeled S in Fig. 14b and c) to be observed at K = 37 MPa $\sqrt{m}$ followed by the formation of a small, V-shaped crack along the slip line at K = 38 MPa $\sqrt{m}$. The V-shaped crack extended by following microcracks formed ahead of the main crack along the slip band at K = 40 MPa $\sqrt{m}$ to produce unstable crack extension for the TL specimen. Void formation and coalescence appear to have produced the microcrack that leads to unstable crack propagation for the TL specimen. Initial crack extension from a blunted crack that had exhibited no prior crack advance was also observed in Fig. 15a and b for the SL orientation at K = 35–38 MPa $\sqrt{m}$ by slip band decohesion. After loading the SL specimen to K = 38.5 MPa $\sqrt{m}$, unstable crack propagation with decreasing fracture resistance at K = 34–35 MPa $\sqrt{m}$ was observed in Fig. 15 for the SL specimen by void formation and coalescence along lath boundaries to produce microcracks ahead of the crack tip that eventually linked to the main crack.

The in situ examinations indicate there was little or no crack advance by crack propagation along the slip bands for beta-treated Zircaloy-4. Unstable crack propagation was observed to occur by void formation along the lath boundaries ahead of the crack tip. This crack propagation resulted from the coalescence of voids along the lath boundaries to produce microcracks that grew to link-up with the main crack. Metallographic examinations from the plastic zone at the mid-thickness of the CT specimens show in Fig. 16 the cracking occurred by void nucleation, growth and coalescence along the lath boundaries. The voids nucleated from Laves phase particles that were initially present at the lath boundaries for beta-treated Zircaloy-4. Void nucleation, growth, and coalescence along the lath boundaries resulted in a crack path that is primarily interlath along the lath boundaries. Fractography of the beta-treated Zircaloy-4 CT specimens shows in Fig. 17 that the crack path is indeed interlath along the lath boundaries. The higher magnification image shows in Fig. 17b the small voids formed at

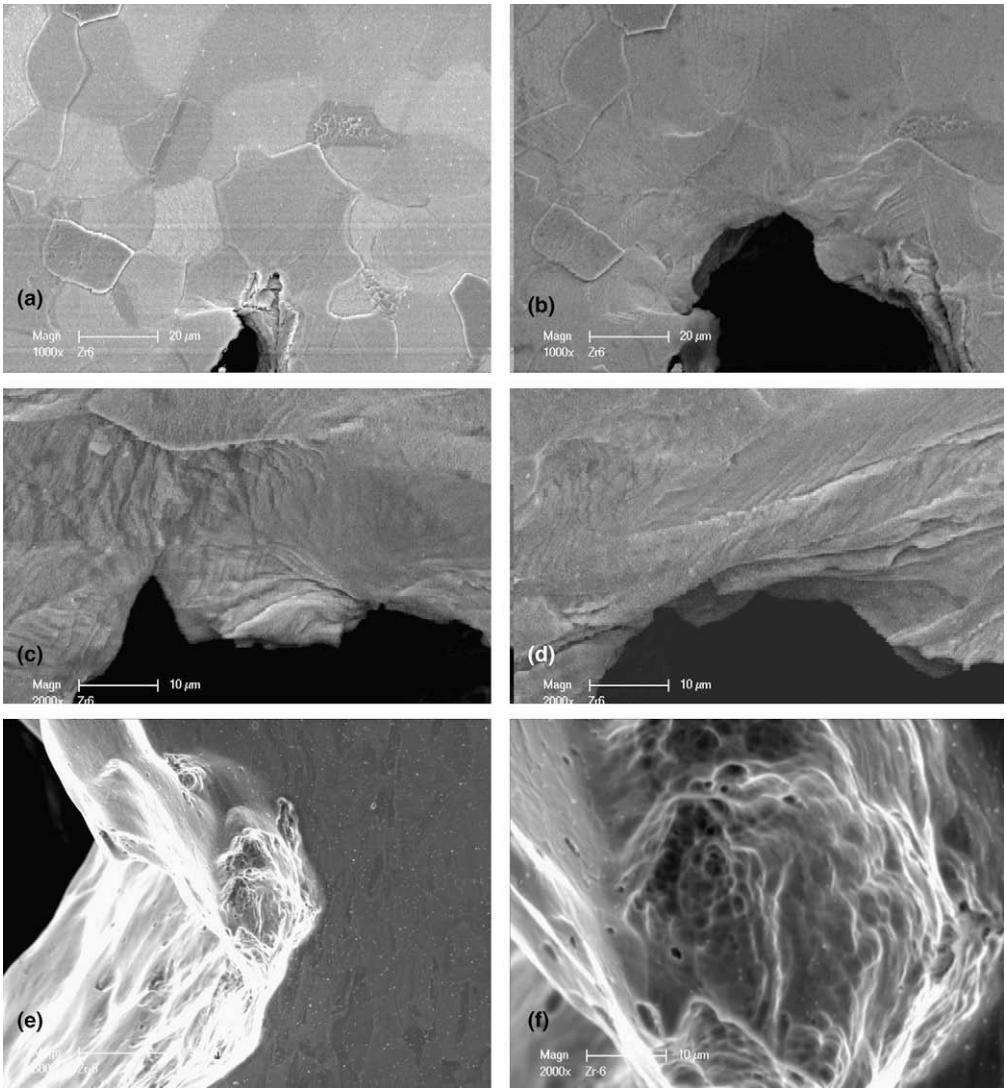

Fig. 10. Processes for crack extension observed for an alpha-annealed Zircaloy-4 CT specimen in the SL orientation (Zr-6) tested at 316 °C: (a) slip band formation with cracking along the slip band, (b) shearing and blunting into a rounded crack tip, (c) decohesion of a slipline emitted from the crack tip to form a small V-shaped microcrack at the crack front, (d) shearing and tearing at the V-shaped microcrack resulting in a large crack opening and a blunted crack tip, (e) SEM from the interior of the crack tip showing voids and microcracks in the near-tip region, and (f) higher magnification of (e).

the fracture surface resulting from void coalescence. Fracture along lath boundaries was previously observed for beta-treated Zircaloy-4 fracture toughness specimens, and the fracture mechanism also was reported to consist of void nucleation and coalescence for Zircaloy-4 [4,8–11,19–22,31,32]. Although the nucleation, growth, and coalescence of voids is a ductile failure mechanism where a high level of fracture energy is absorbed, rapid operation of this process at lath boundaries results in unstable crack propagation with no rising *K*-resistance curve for beta-treated Zircaloy-4 in all orientations.

4. Results and discussion for in situ tensile testing

In situ tensile testing was performed at room-temperature using a smooth tapered specimen so that the deformation would be localized to a region that could be located and observed easily in the SEM. The use of a tapered tensile specimen may result in an increase in scatter in the tensile data shown in Fig. 18, and summarized in Table 4. The tensile specimens could only be pulled to approximately 5–10% total strain in situ before the maximum displacement travel in the SEM loading stage was reached. Only the formation of slip lines were observed at these strain levels, and void formation was not observed to occur in any of the specimens. The tensile tests were continued in an MTS testing machine at room-temperature outside the SEM to achieve higher strain levels, and the surfaces were examined in the SEM just after the maximum load or Ultimate Tensile Stress (UTS) was achieved but prior to the final fracture. One tensile specimen (Zr-8) was intentionally pulled to failure to observe the failure mechanism.

The stress–strain curves for alpha-annealed Zircaloy-4 are shown in Fig. 18a. There is scatter in the tensile properties with respect to orientation and for the duplicate tests in the transverse orientation shown in Fig. 18a and Table 4 with low yield strength and rapid strain hardening at low strains in the LT orientation. The two tests in the TL orientation exhibited very different tensile results. The large scatter in tensile properties observed in all orientations for alpha-annealed is likely attributed to a local variation in microstructure and texture in the local taper region of the tensile specimen where the deformation was localized rather than a measure of the macroscopic variability in tensile properties. An unusual observation of a sudden increase in strain hardening was

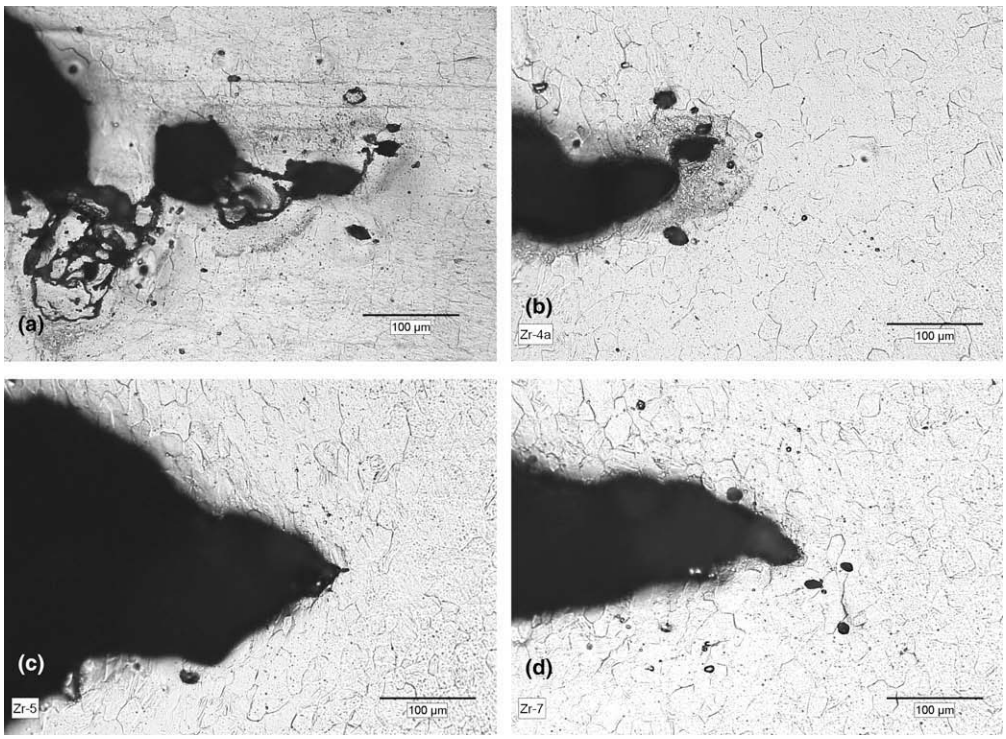

Fig. 11. Metallographic sections from alpha-annealed Zircaloy-4 CT specimens tested at room-temperature from the plastic zone at the crack tip in the center of the specimen showing a crack growth mechanism of void nucleation, void growth, and coalescence: (a) LT specimen at mid-thickness, (b) LT specimen at 50–100 μm below mid-thickness, (c) void-like crack at tip in the TL specimen, and (d) SL specimen showing voids ahead of the crack tip.

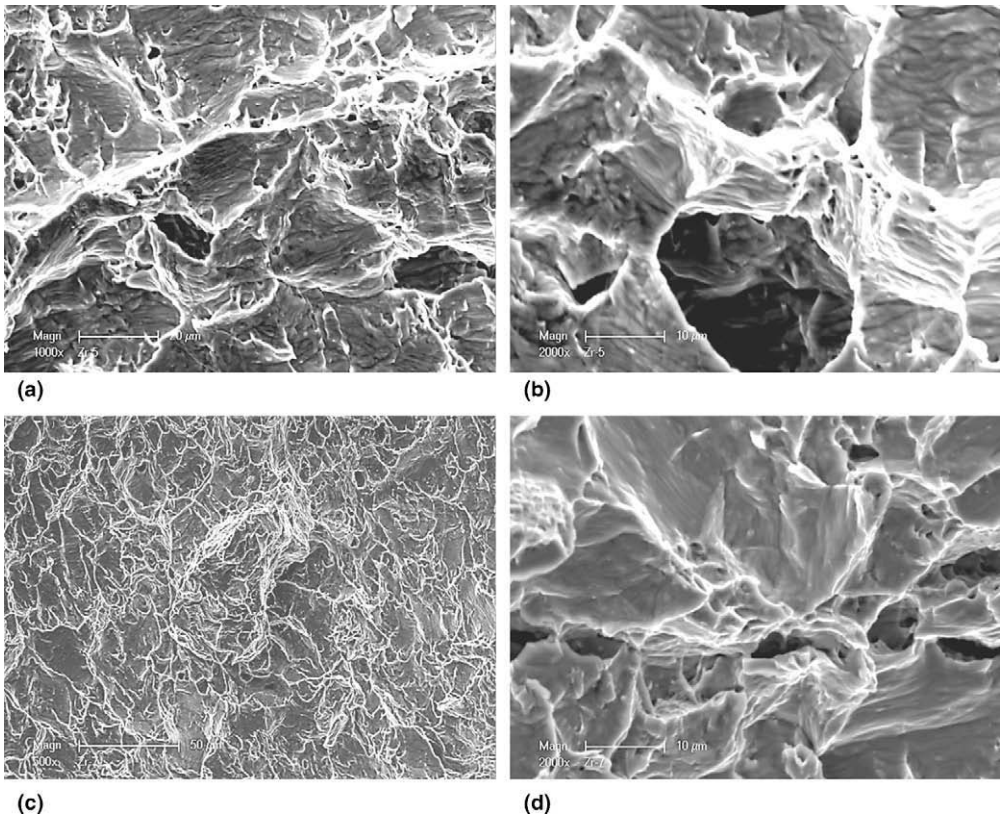

Fig. 12. Fractography from the fracture surfaces of alpha-annealed Zircaloy-4 CT specimens tested at room-temperature: (a) TL specimen showing wavy slip at grain surfaces and voids formed at small particles, (b) TL specimen at higher magnification showing a row of small voids that have formed on a tear ridge, (c) SL specimen showing dimples and tear ridges, and (d) SL specimen showing small voids formed on tear ridges.

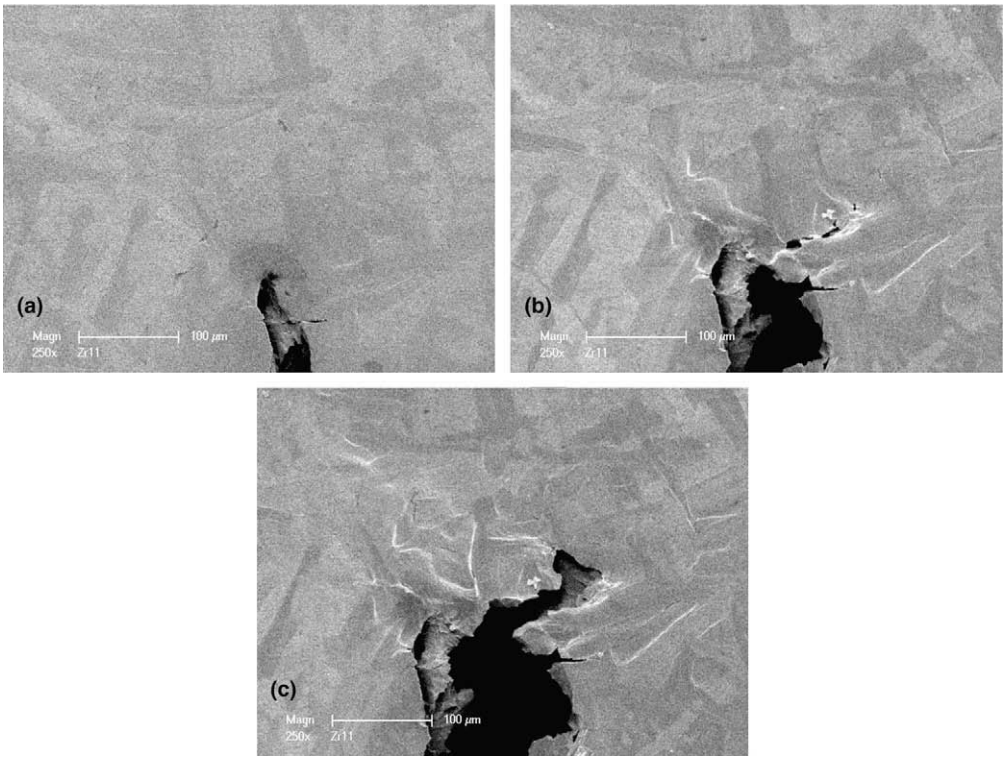

Fig. 13. Processes for crack extension observed for the beta-treated Zircaloy-4 CT specimen in the LT orientation (Zr-11) tested at room-temperature: (a) blunted crack tip at 35 MPa $\sqrt{m}$, (b) shear band and void formation along the boundaries between lath grains at 40 MPa $\sqrt{m}$, and (c) fracture of ligaments ahead of the crack tip occurring at K = 40 MPa $\sqrt{m}$.

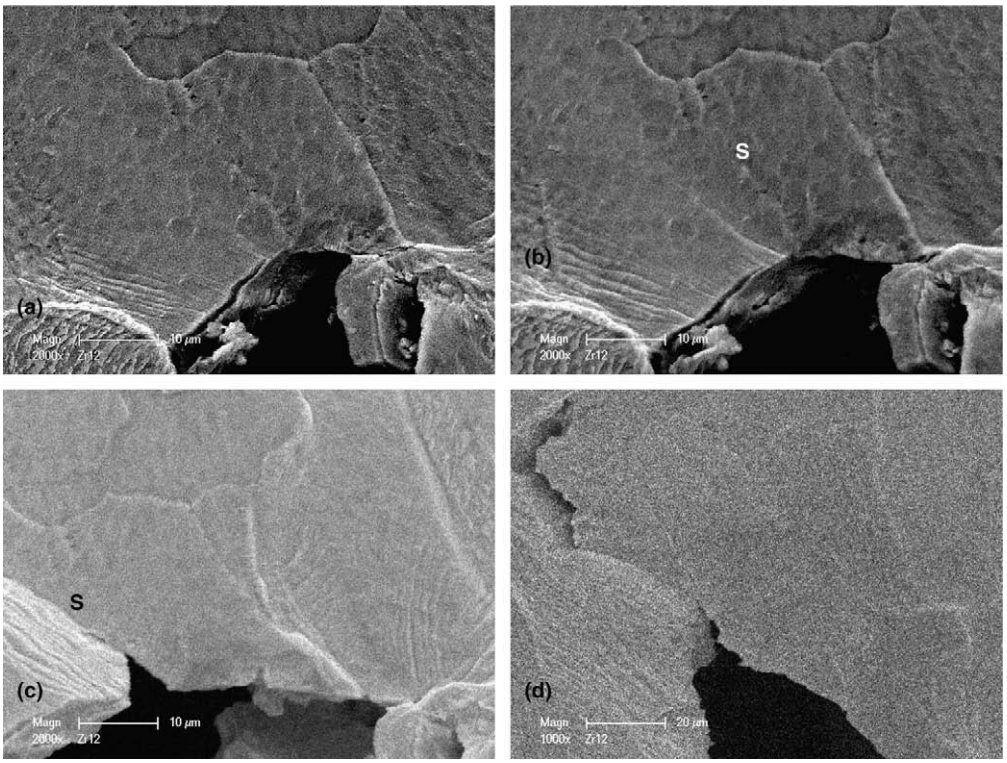

Fig. 14. Crack extension observed for the beta-treated Zircaloy-4 CT specimen in the TL orientation (Zr-12) tested at room-temperature: (a) blunted crack tip at K = 37 MPa $\sqrt{m}$, (b) deformation localized along a shear band (marked S) at the crack tip at 37 MPa $\sqrt{m}$, (c) slip band decohesion to form V-shaped cracks along the crack front at K = 38 MPa $\sqrt{m}$, and (d) microcrack formation ahead of the V-shaped crack at K = 40 MPa $\sqrt{m}$.

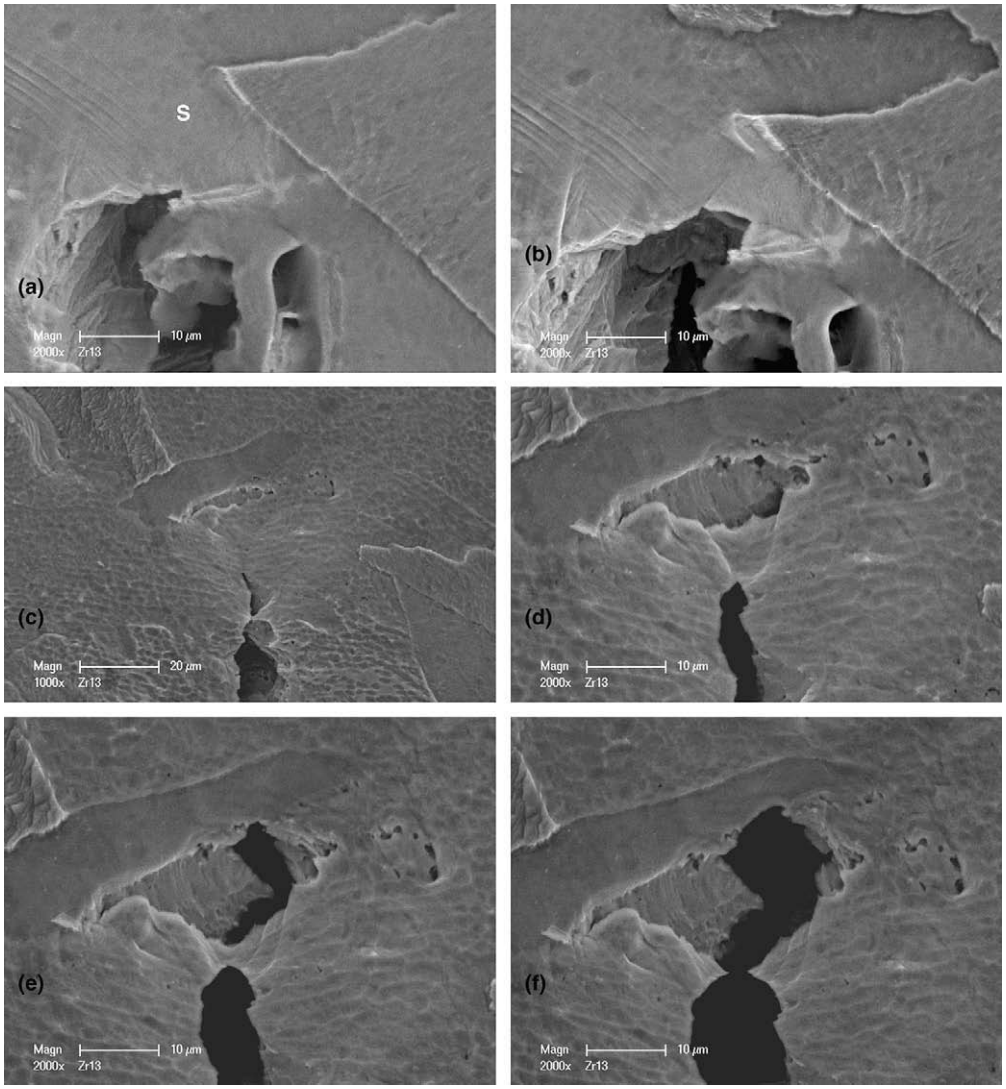

Fig. 15. Crack extension observed for the beta-treated Zircaloy-4 CT specimen in the SL orientation (Zr-13) tested at room-temperature: (a) crack extension along a shear band at the blunted crack tip at K = 35 MPa $\sqrt{m}$, (b) crack advance along shear bands with void formation at 38 MPa $\sqrt{m}$, (c) void nucleation at crack tip at lower K = 34 MPa $\sqrt{m}$, (d) void growth at multiple sites at 34 MPa $\sqrt{m}$, (e) cavitated zone from the coalescence of multiple voids at 34 MPa $\sqrt{m}$, and (f) crack tip joined with voids leading to unstable fracture at K = 35 MPa $\sqrt{m}$.

observed for the SL orientation, but the highest UTS and total elongation were observed for this orientation. Although slip may be more difficult to initiate in the SL orientation for alpha-annealed Zircaloy-4 when the material is not constrained, higher ultimate tensile strength and total strain values may be reached. The more uniform texture and microstructure for beta-treated Zircaloy-4 results in more consistent tensile results shown in Fig. 18b with the exception of slightly higher tensile strength and lower elongation in the SL orientation. This difference in tensile data between the SL orientation compared to the LT and TL orientations for beta-treated Zircaloy-4 may result from some residual texture or structure remaining after the heat treatment, but likely represents scatter in results for the tapered specimens. The fracture toughness results for beta-treated Zircaloy-4 were generally more isotropic with respect to orientation than the tensile results. In general, both the yield strength and total elongation values for beta-treated Zircaloy-4 were slightly lower than those for alpha-annealed Zircaloy-4. This is consistent with the slightly higher toughness values observed for alpha-annealed Zircaloy-4 as compared to beta-treated.

For alpha-annealed Zircaloy-4, the deformed surfaces of the tensile specimens were covered with slip bands and voids that did not appear at stresses below the UTS. Void formation was observed in Fig. 19 at the surface of the alpha-annealed Zircaloy-4 tensile specimens after the UTS had been reached. Since necking generally occurs at the UTS, this indicates the triaxial stress-state at the neck results in strain-localization that promotes void formation. The voids are observed to form at impinging slip bands from neighboring grains, slip band intersections at grain boundaries, and slip band intersections with Laves phase particles. Large voids are formed by the growth and coalescence of neighboring voids, see Fig. 19c. This suggests the process of void nucleation, growth, and coalescence for alpha-annealed Zircaloy-4 observed in the tensile specimens at the point of flow localization is similar to that observed at the point of unstable crack propagation in the pre-cracked CT specimens.

The void nucleation process in the beta-treated Zircaloy-4 tensile specimens also was observed to occur at the UTS and beyond, but Fig. 20 shows void nucleation occurred most often at lath boundaries by impinging slip bands. Void nucleation may also

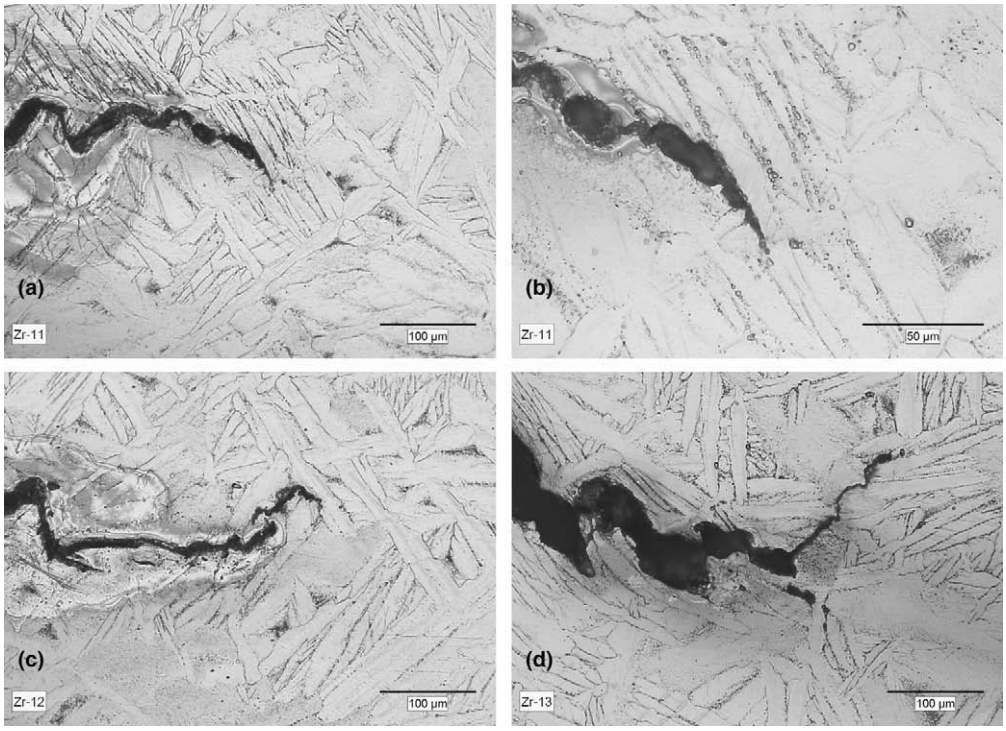

Fig. 16. Metallographic sections from beta-treated Zircaloy-4 CT specimens tested at room-temperature from the plastic zone at the crack tip in the center of the specimen showing a crack growth mechanism in advance of the crack tip involving void nucleation, void growth, and coalescence starting from $Zr(Fe,Cr)_2$ particles along the lath grain boundaries: (a) LT specimen showing void nucleation, growth, and coalescence along lath boundaries, (b) higher magnification image from the LT specimen showing void nucleation at $Zr(Fe,Cr)_2$ particles along the lath boundaries, (c) TL specimen showing void nucleation, growth, and coalescence, and (d) void nucleation, growth and coalescence occurring in the SL specimen.

occur within the lath at the intersection of slip bands. Void coalescence generally resulted in the formation of larger voids or microcracks. Many lath boundaries were observed to be dotted with rows of micron-sized voids, whose coalescence eventually would lead to the formation of a grain boundary microcrack. The same process of void formation and coalescence at lath boundaries observed for the tensile specimens was also observed in the LT, TL, and SL orientations of the pre-cracked CT specimens for beta-treated Zircaloy-4.

In situ observations from both the tensile and CT specimens show the fracture mechanisms in both alpha-annealed and beta-treated Zircaloy-4 occurs by tearing along localized slip bands at low stress and low K values in the rising part of the K-resistance curve, and the nucleation, growth, and coalescence of voids and their subsequent linkage with the main crack generally occurs at the point of unstable crack propagation in the K-resistance curves and at the point of flow localization at the UTS in the stress–strain curves. Void nucleation, growth and coalescence was observed for the pre-cracked CT specimens of alpha-annealed Zircaloy-4 at both room-temperature and 316 °C. This same mechanism was also observed for the pre-cracked CT specimens and tensile specimens for both alpha-annealed and beta-treated Zircaloy-4 tested at room-temperature, suggesting the same mechanism operates from room-temperature to 316 °C in all cases.

5. Modeling

Unstable crack propagation was observed to occur in both alpha-annealed and beta-treated Zircaloy-4 by a multi-step process of void nucleation, growth, and coalescence. Dimples of various sizes were observed at the fracture surface near and far away from the crack tip, indicating a void nucleation, growth and coalescence process had occurred. Metallographic examinations of the CT specimens and the surface of tensile specimens showed the voids were nucleated primarily from the small Laves phase particles present in both alpha-annealed and beta-treated Zircaloy-4 by slip band impingement. Thus, micromechanical modeling was focused on treating void nucleation, growth, and coalescence at the Laves phase particles under the influence of a slip band or dominant crack.

5.1. Void nucleation

Experimental evidence shows that void nucleation in the zirconium alloys studied occurs by slip impingement at particles located within grains or at grain boundaries. Thus, the model for void nucleation considered a dislocation pileup impinging at a hard intermetallic particle, as shown in Fig. 21a. The hard particle is assumed to be a Laves phase intermetallic such as $ZrCr_2$, $ZrFe_2$, or $Zr(Cr,Fe)_2$ with the C14 or C15 structure. Plastic deformation in the Zr-alloy matrix results in the generation of dislocations that pile up against hard particles that resist dislocation motion. Most of the plastic energy is dissipated as heat, but a small amount of the energy is stored as elastic strain energy in the dislocations and part of this stored energy is released in creating the new surfaces during void nucleation at the particle. The Gibbs Free Energy, ΔG, change associated with the nucleation of a crack in the particle is [33]:

$$\Delta G = -W_e - W_m + 2c\gamma_s \tag{1}$$

where W_e is the elastic strain energy stored in dislocations, W_m is the mechanical energy released due to the opening of a crack, c is the half-length of the incipient crack in the particle, Fig. 21b, or the projected-half-length of the incipient interface crack, Fig. 21c, and γ_s is the appropriate surface energy of the particle or the particle/matrix interface.

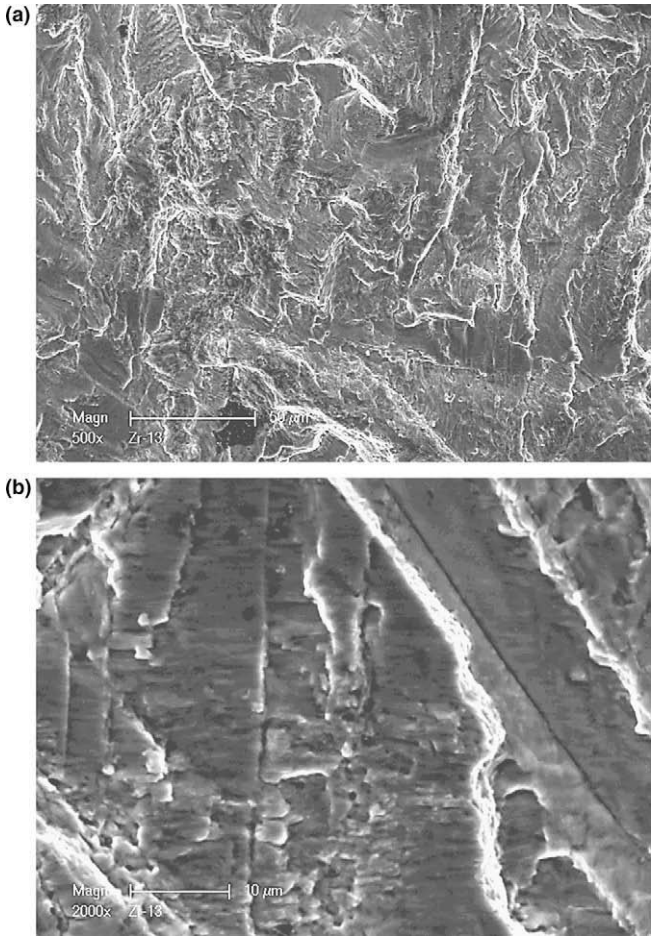

Fig. 17. Fractography from the fracture surfaces of a SL beta-treated Zircaloy-4 CT specimen tested at room-temperature: (a) lower magnification image of the surface resulting from crack propagation along the lath boundaries, and (b) higher magnification image of internal microcracks and voids formed at the lath boundaries.

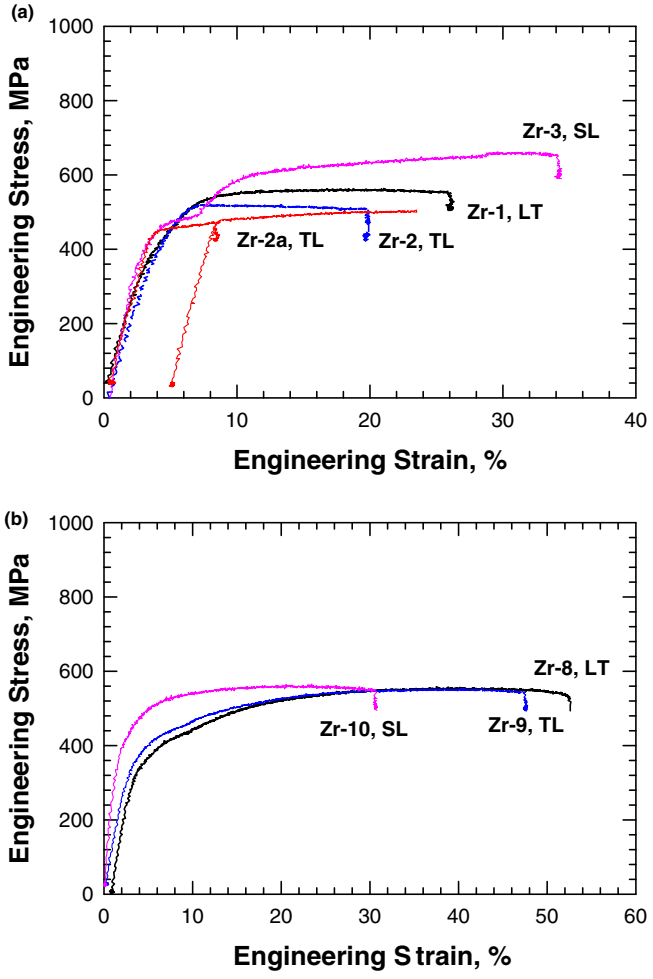

Fig. 18. Engineering stress–strain curves measured at room-temperature in the longitudinal (LT), transverse (TL), and through thickness (SL) orientation for: (a) alpha-annealed Zircaloy-4, and (b) beta-treated Zircaloy-4.

Eq. (1) has been used previously to derive an expression for treating crack initiation by slip impingement at a hard particle under fatigue loading [33]. The same procedure was applied for monotonic loading by replacing the stress range by the stress and taking the number of fatigue cycles to be one. Applying these changes to Eq. (27) from [33], the resulting expression for crack initiation by slip impingement at a hard particle under monotonic tensile loading is obtained, resulting in

$$\sigma - \sigma_y = \left[\frac{8(\mu+\mu')}{\lambda\mu'}\right]^{1/2}\left[\frac{M\mu h^2}{d(h+d)}\right]\left[\frac{c}{\xi}\right] \tag{2}$$

where σ is stress, σ_y is yield stress, M is the Taylor factor, h is slip band spacing, d is grain size, ξ is particle size, μ is the shear modulus of matrix, and μ' is the shear modulus of the particle. The parameter λ accounts for interactions of dislocation pileups under fatigue loading. For monotonic loading, λ can be taken to be unity since no stored energy is lost to irreversible dislocation interactions under cyclic loading. By taking $2c = \xi$, where c is the half-length of the incipient crack in the particle so that this term becomes unity, and rearranging the terms, Eq. (2) becomes

$$\sigma = \sigma_y\left\{\left[\frac{8(\mu+\mu')}{\mu'}\right]^{1/2}\left[\frac{M\mu h^2}{\sigma_y d(h+d)}\right]+1\right\} \tag{3}$$

and the plastic strain, ε_p, for initiating a particle-sized crack or void at the particle is given by

$$\varepsilon_p = \left\{\frac{\sigma_y}{k}\left\{\left[\frac{8(\mu+\mu')}{\mu'}\right]^{1/2}\left[\frac{M\mu h^2}{\sigma_y d(h+d)}\right]+1\right\}\right\}^{1/N} \tag{4}$$

after stress is related to the plastic strain via the following power-law relation

$$\sigma = k\varepsilon_p^N \tag{5}$$

Eq. (4) was utilized to predict the plastic strain for the initiation of particle-sized voids either by particle cracking or interface decohesion at Laves phase particles in a Zr-alloy matrix. The shear modulus was computed from the Young's modulus and Poisson's ratio using properties of Zircaloy-4 and the Laves phase particles. Theoretical values of Laves phase properties were obtained from first-principles computations from the literature [34]. The parameters k and σ_y were determined from tensile data (Table 4). The slip line spacing was determined from micrographs of tensile specimens. The grain size was determined from the OIM results in Table 2. Average values of k, σ_y, h, and d were obtained from experiments performed during this investigation. They were used in conjunction with Eq. (4) for the void strain computation. Table 5 is a summary of the material input and the predicted plastic strains at void nucleation for alpha-annealed and beta-treated Zircaloy-4. The computed void initiation strains are on the order of 12–27% for the average tensile properties, slip band spacing, and grain size. This calculated strain level is within the range of strain measured

Table 4
Summary of the tensile properties and the material constants in the Ramberg–Osgood constitutive relation for individual specimens.

Spec./orient	σ_y (MPa)	σ_{UTS} (MPa)	E (GPa)	N	n	σ_y	K (MPa)	α	Fracture strain [%]	Fract. mech.
Alpha-annealed										
Zr-1/LT	365.3	506.7	99.3	0.167	5.99	0.00368	872.2	1.483	53.50	a
Zr-2/TL	354.9	513.1	99.3	0.1	10.00	0.00357	703.0	0.301	>26.40	a
Zr-2a/TL	420.0	501.6	99.3	0.2	5.00	0.00423	835.91	7.571	69.30	a
Zr-3/SL	362.8	602.3	99.3	0.279	3.58	0.00365	1205.5	3.699	55.40	a
Beta-treated										
Zr-8/LT	327.3	552.8	99.3	0.364	2.75	0.00330	1130.7	10.067	45.40	b
Zr-9/TL	327.9	553.6	99.3	0.32	3.13	0.00330	1069.0	7.540	43.90	b
Zr-10/SL	345.4	556.6	99.3	0.189	5.29	0.00348	903.6	1.773	31.50	b

a: Voids within grains and at grain boundaries.
b: Grain boundary voids and microcracks.

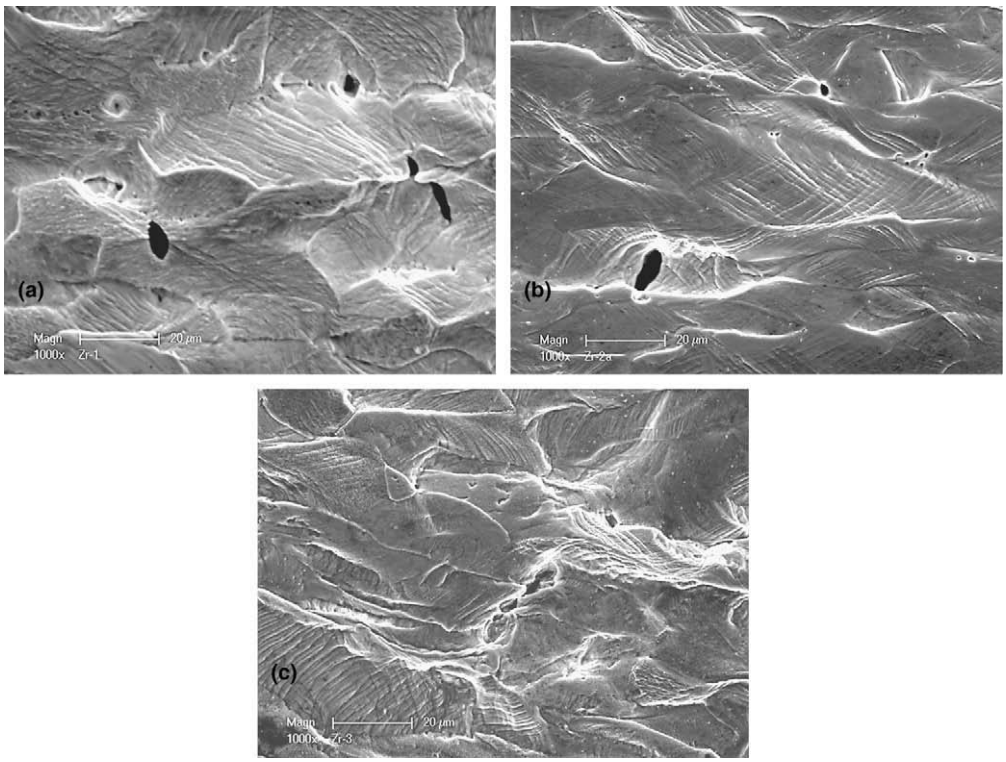

Fig. 19. SEM images of voids observed on the surface of alpha-annealed tensile specimens after loading at or past the ultimate stress: (a) longitudinal or LT (Zr-1) orientation, (b) transverse or TL (Zr-2a) orientation, and (c) through thickness or SL (Zr-3) orientation.

on the actual tensile specimens in Table 4 at which void nucleation was observed, suggesting the model is self-consistent. The void initiation strain is sensitive to the slip band spacing, h, and the grain size, d, because they dictate the slip uniformity and the storage energy in the dislocation pile up.

5.2. Crack tip void growth and coalescence

The model for void growth and coalescence ahead of the crack tip was based on an approach taken for stainless steels where the ductile tearing process also was controlled by the growth and coalescence of voids initiated at hard inclusions [35]. This void growth-based fracture model was formulated by considering a one-dimensional array of voids of the size equal to the average particle size in font of the crack tip, as shown in Fig. 22. Based on the results from the previous section, void nucleation is assumed to occur at low loads or low plastic strains so that fracture is dominated by the growth and coalescence of voids with the crack tip in an elastic–plastic material.

Following the approach proposed by Saxena et al. [35], void growth and coalescence was assumed to occur ahead of the crack tip under J-controlled conditions with a near- tip field derived by the Hutchinson–Rice–Rosengren (HRR) field [36,37], where J is Rice's J-integral [38]. In the J-controlled regime, the incremental change in the near-tip strain $d\varepsilon$ due to an incremental increase in the J-integral, dJ, is given by [35]

$$\frac{d\varepsilon}{\varepsilon} = \frac{n}{n+1}\frac{dJ}{J} \tag{6}$$

and the strain ε in the HRR field is given by

$$\varepsilon = \alpha\varepsilon_y\left[\frac{J}{\alpha I_n \sigma_y \varepsilon_y r}\right]^{\frac{n}{n+1}}\tilde{\varepsilon}(\theta) \tag{7}$$

where r is distance from the crack tip, ε_y is the yield strain, and σ_y is the yield stress. The parameter n is the inverse of the strain-hardening exponent and α is the material constant in the Ramberg–Osgood constitutive relation. Since the HRR field quantities are based on the

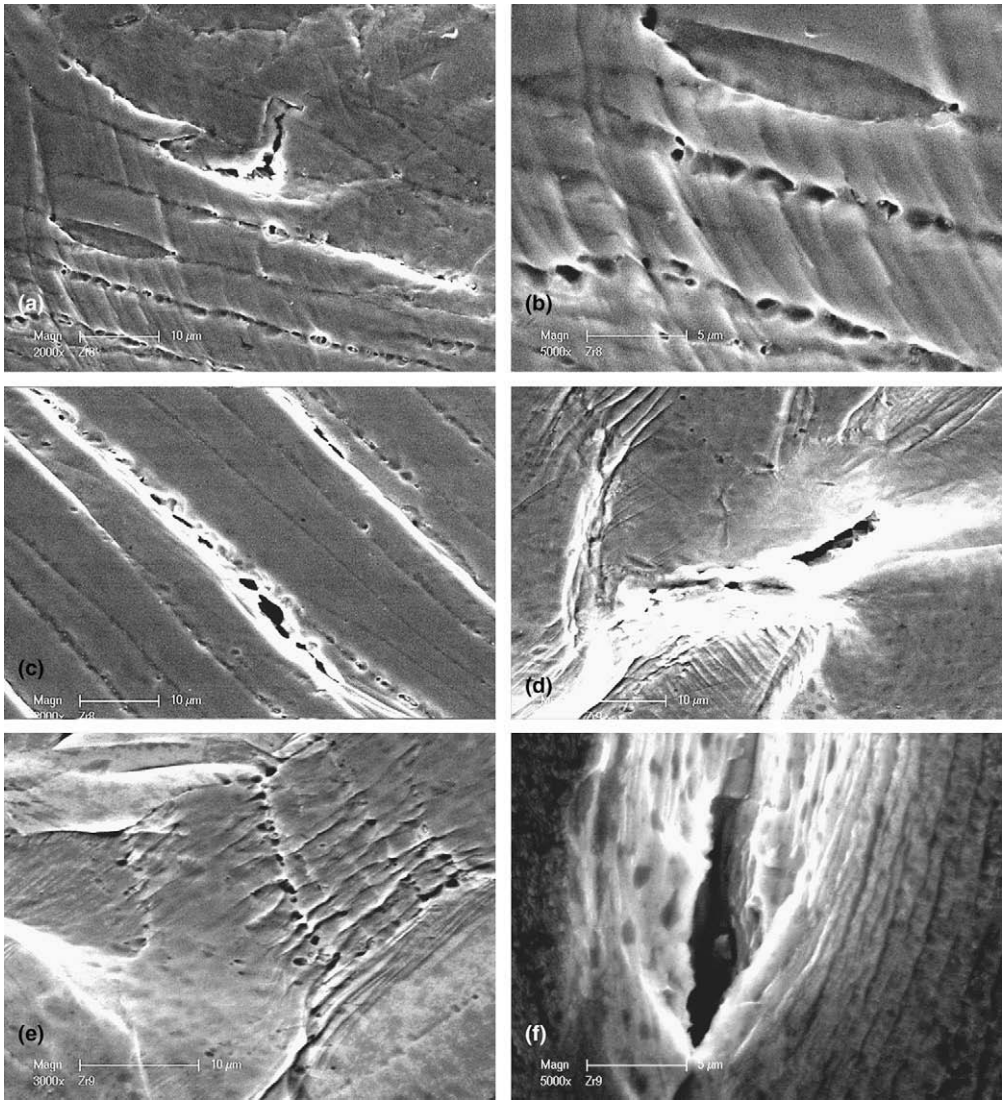

Fig. 20. SEM images of voids observed on the surface of beta-treated tensile specimens after the specimens were loaded to or past the ultimate stress: (a) slip induced voids in LT specimen, (b) small particles within voids for LT, (c) microcrack formed by void coalescence for TL orientation, (d) void nucleation, growth, and coalescence to produce a microcrack along a lath boundary in the SL orientation, (e) row of voids in SL form interesting slip bands, and (f) microcrack formed by slip band decohesion in SL with small voids formed within the slip band.

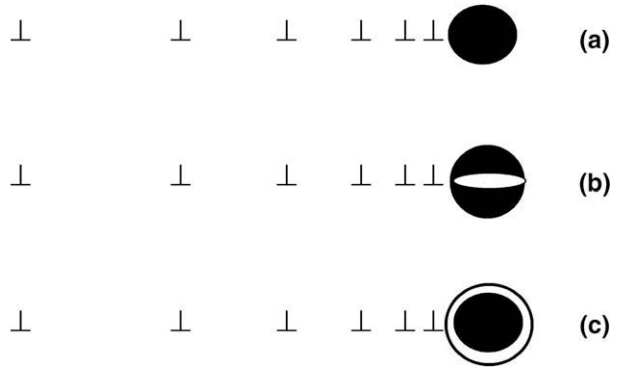

Fig. 21. Void formation by slip impingement at particles leading to interface decohesion or particle cracking: (a) slip impingement at a particle, (b) particle cracking, and (c) interface decohesion.

Ramberg–Osgood constitutive relationship, the Ramberg–Osgood parameters were determined and used for this model. The HRR field quantities I_n and $\tilde{\varepsilon}(\theta)$ are listed in tables by Shih [39] for different stress state, n value, and angle, θ, from the crack plane. Substituting Eq. (7) into Eq. (6) leads one to

$$\int_0^{\varepsilon_c} d\varepsilon = \int_0^{J_c} \frac{n}{n+1}\alpha\varepsilon_y\left(\frac{J}{\alpha\sigma_y\varepsilon_y I_n r}\right)^{\frac{n}{n+1}}\tilde{\varepsilon}(\theta)\frac{dJ}{J} \tag{8}$$

where ε_c is the critical strain necessary to grow the first void ahead of the crack tip to the critical void size for linking with the crack tip. If the void coalescence with the crack tip occurs at $r = \Lambda$ taken to be the void spacing (Fig. 23), then Eq. (8) can be integrated and rearranged to give

$$J_c = \left[\frac{\varepsilon_c}{\alpha\varepsilon_y\tilde{\varepsilon}(\theta)}\right]^{\frac{n}{n+1}}(\alpha\sigma_y\varepsilon_y I_n\Lambda) \tag{9}$$

as the critical J-integral for the onset of crack growth. For fracture by ductile void growth, the critical fracture strain can be obtained on the basis of the treatment of void growth kinetics for an isolated void in a triaxial stress field derived by Rice and Tracey [40]. According to this model, the void expansion rate is given by [40]

Table 5
Summary of the model constants and the predicted void nucleation strain (Eq. (4)) at cubic (C15) or hexagonal (C14) Laves phase $ZrCr_2$, ZrFe, or $Zr(Cr,Fe)_2$ particles by slip band impingement in alpha-annealed and beta-treated Zircaloy-4.

Particle	E (GPa)	v	G (GPa)	N	k (MPa)	G(Zr) (GPa)	h (μm)	d (μm)	σ_y (MPa)	Void initiation strain (%)
Alpha-annealed Zircaloy-4										
Cubic $ZrCr_2$	153	0.356	56.42	0.364	1130	37.33	1.58	15	365.3	15.97
Cubic $CrFe_2$	175	0.301	67.26	0.364	1130	37.33	1.58	15	365.3	14.74
Hexagonal $ZrCr_2$	263	0.141	115.25	0.364	1130	37.33	1.58	15	365.3	12.15
Beta-treated Zircaloy-4										
Cubic $ZrCr_2$	153	0.356	56.42	0.364	1130	37.33	1.77	15	365.3	27.10
Cubic $CrFe_2$	175	0.301	67.26	0.364	1130	37.33	1.77	15	365.3	24.96
Hexagonal $ZrCr_2$	263	0.141	115.25	0.364	1130	37.33	1.77	15	365.3	20.48

$$\frac{dR}{R} = 0.322 d\bar{\varepsilon} \exp\left(\frac{1.5\sigma_m}{\bar{\sigma}}\right) \tag{10}$$

where R is the void radius, σ_m is the mean stress, and $\bar{\varepsilon}$ and $\bar{\sigma}$ are von Mises effective strain and stress, respectively. Integrating Eq. (10) to the critical strain leads one to

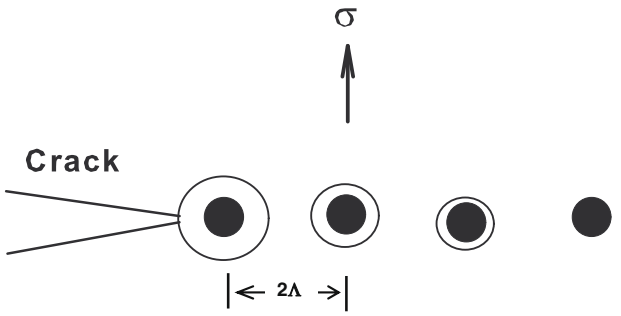

Fig. 22. Void nucleation, growth, and coalescence ahead of a crack tip. The linkage of crack tip with voids results in crack extension.

$$\varepsilon_c = \frac{\ln(R_c/R_o)}{0.322 \exp(1.5\sigma_m/\bar{\sigma})} \tag{11}$$

which can be combined with Eq. (9) to obtain

$$J_c = \left[\frac{\ln(R_c/R_o)}{0.322\alpha\varepsilon_y\bar{\varepsilon}(\theta)\exp(1.5\sigma_m/\bar{\sigma})}\right]^{\frac{n}{n+1}} (\alpha\sigma_y\varepsilon_y I_n \Lambda) \tag{12}$$

where R_c and R_o are the critical and initial void radius, respectively.

The crack extension at J_c, which results from linking of the first void radius to the crack tip, is taken to be the void spacing, Λ (Fig. 22), that is also assumed to be the distance to the void from the crack tip The strain level ε_i at the next void is given by Eq. (7) with $r = 2\Lambda$ and the corresponding void radius R_i is given by

$$R_i = R_o \exp[0.322\varepsilon_i \exp(1.5\sigma_m/\bar{\sigma})] \tag{13}$$

and the amount of strain required to reach the critical strain for void growth at the next void from R_i to R_c is

$$\Delta\varepsilon_i^c = \frac{\ln R_c/R_i}{0.322 \exp(1.5\sigma_m/\bar{\sigma})} \tag{14}$$

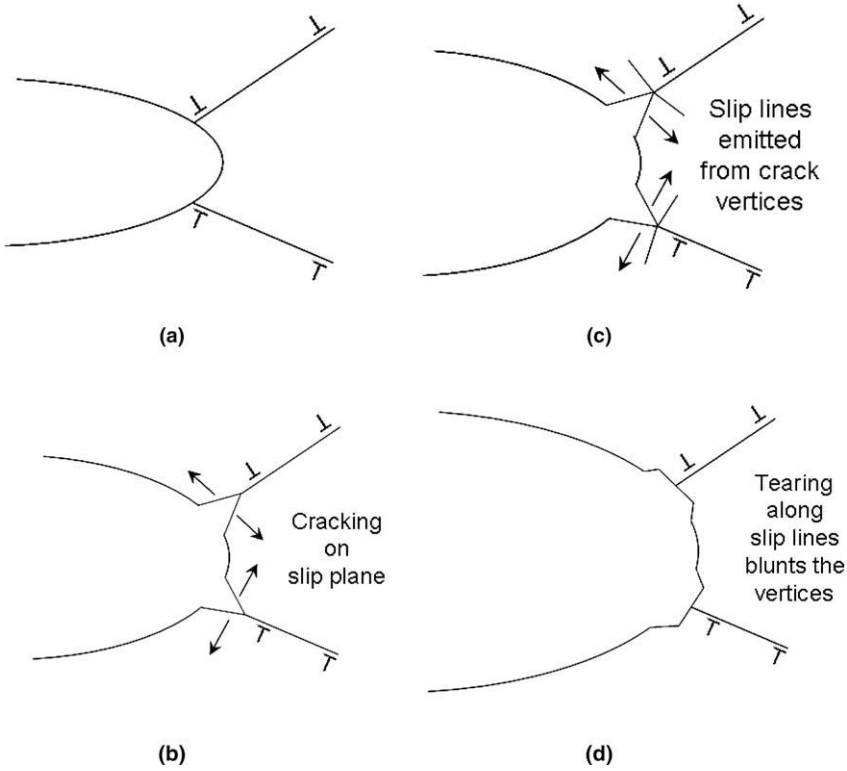

Fig. 23. Crack growth mechanism by slip band emission, decohesion of slip band, and crack tip blunting by tearing along slip band: (a) slip emission from a round crack tip, (b) decohesion of slip lines to form V-shaped crack vertices, (c) slip lines emitted from V-shaped vertices, and (d) tearing along slip lines blunts the vertices.

That strain is supplied by increasing the applied J-integral from J_c to J_i. From Eq. (9), the strain available for further void growth and coalescence at the next void due to an increase in the J-integral is obtained as

$$\Delta\varepsilon_i^c = \alpha\varepsilon_y\tilde{\varepsilon}(\theta)\left(\frac{1}{\alpha\sigma_y\varepsilon_y I_n\Lambda}\right)^{\frac{n}{n+1}}\left(J_i^{n/(n+1)} - J_c^{n/(n+1)}\right) \tag{15}$$

which can be combined with Eq. (14) to give

$$J_i = \left[J_c^{n/(n+1)} + \left(\frac{\ln(R_c/R_i)}{0.322\alpha\varepsilon_y\tilde{\varepsilon}(\theta)\exp(1.5\sigma_m/\bar{\sigma})}\right)(\alpha\sigma_y\varepsilon_y I_n\Lambda)^{n/(n+1)}\right]^{\frac{n+1}{n}} \tag{16}$$

and the corresponding stress intensity factor, K_i, for the plane strain condition is

$$K_i = \left[\frac{EJ_i}{(1-\nu^2)}\right]^{1/2} \tag{17}$$

for a crack extension which results from the growth and linkage of the ith void with the crack tip. That increment of extension is given by

$$\Delta a = (1+i)\Lambda \tag{18}$$

For the plane stress condition, the $(1-\nu^2)$ term in Eq. (17) is replaced by 1. A rising J-resistance or K-resistance curve is obtained as long as $\Delta\varepsilon_i^c > 0$ or $R_c/R_i > 1$.

5.3. Model predictions compared to experimental results

Eqs. (16)–(18) were utilized to compute J_R and K_R curves for both alpha-annealed and beta-treated Zircaloy-4 based on characterization of the microstructure and measurements of slip band spacing and void size and spacing made from the tensile specimens. Crack growth was assumed to occur directly ahead of the crack tip with $\theta = 0$ under plane strain conditions. The parameters in the Ramberg–Osgood constitutive relation were obtained from the conventional tensile stress–strain curves. The initial void radius, R_o, was taken to be the Laves phase particle radius measured on SEM micrographs of the tensile specimen, while the critical void radius was taken as the void radius where void coalescence occurred in a row of aligned voids. The latter turned out to correspond to the slip band spacing. The fact that the void spacing is equivalent to the slip band spacing is somewhat fortuitous, but could be explained by the fact that the dislocations arise from the elastic mismatch between the particle and matrix. The back stresses resulting from slip band intersection with a barrier could result in void initiation at the Laves phase particles. More investigation is needed to understand the exact mechanism for void nucleation. The ratio of mean stress to effective stress is 3 for perfectly plastic materials, but it can be higher for strain-hardening materials. Numerical simulations of void growth [41] showed that the triaxial stress ratio ranges from 3 to 4.2 for $N = 0.2$. Thus, a triaxial stress ratio of 3.25 was used the J_R and K_R curve computation. Eq. (9) was utilized In the J_R and K_R curve computations to compute J_c at the onset of crack growth. Then J_i and da were computed using Eqs. (16) and (18). Subsequently, K_c and K_i were computed from J_c and J_i using Eq. (17). A summary of the model constants utilized in these computations is presented in Table 6.

Comparison of the computed and measured K-resistance curves for alpha-annealed and beta-treated Zircaloy-4 are shown in Figs. 3 and 4, respectively. The onset of unstable crack propagation was generally well predicted for all specimens. For the materials that exhibited a flat K-resistance curve with immediate unstable crack propagation, such as the SL orientation for alpha-annealed Zircaloy-4 and all orientations for beta-treated Zircaloy-4, predictions from the void growth and coalescence model provided excellent matches to the experimentally measured K-resistance curve and K_c and K_{SS} values. The apparent lack of a resistance curve for beta-treated Zircaloy-4 is likely the result of void nucleation and growth occurring at the closely spaced Laves phase particles along the lath boundaries. The void spacing along the lath boundaries is small so that once the voids are nucleated, little growth is required before the voids coalesce to produce unstable crack propagation. In the case of alpha-annealed Zircaloy-4 in the LT and TL orientation, the computed K-resistance curves do not exhibit the rising R-curve behavior observed for these specimens, but the computed K_{SS} values are a close match to the measured values. The Laves phase precipitates present in alpha-annealed Zircaloy-4 are non-uniformly distributed within the grains and at the grain boundaries. The variation in the spacing between precipitates may play a role, as larger spacing between the voids formed at the precipitates would give rise to a more gradually rising K-resistance curve. As discussed in the following section, texture also may play a role in producing the rising R-curve behavior observed in the K-resistance curves for both LT and TL alpha-annealed Zircaloy-4. In the case of SL alpha-annealed Zircaloy-4, higher stress was likely required to produce slip, so that unstable crack extension occurred by a void nucleation and growth process, as illustrated by the close match between the computed and measured K-resistance curve. Thus, the physical implications of the void growth and nucleation model are consistent with unstable crack extension occurring immediately upon reaching J_c in beta-treated Zircaloy-4 and the SL

Table 6
Summary of the material constants in the void growth model and the predicted J_c and K_c at the onset of crack growth by coalescence of the crack tip with the first void for the plane strain condition.

Spec.	σ_y (MPa)	σ_{UTS} (MPa)	E (GPa)	N	n	ε_y	k (MPa)	α
Zr-1	365.3	506.7	99.3	0.167	5.99	0.00368	872.2	1.483
Zr-2	354.9	513.1	99.3	0.1	10.00	0.00357	703	0.301
Zr-2a	420	501.6	99.3	0.2	5.00	0.00423	835.91	7.571
Zr-3	362.8	602.3	99.3	0.279	3.58	0.00365	1205.5	3.699
Zr-8	327.3	552.8	99.3	0.364	2.75	0.00330	1130.7	10.067
Zr-9	327.9	553.6	99.3	0.32	3.13	0.00330	1069	7.540
Zr-10	345.4	556.6	99.3	0.189	5.29	0.00348	903.6	1.773

Spec.	I_n	$\varepsilon_{eff}(n,0)$	σ_m/σ_y	R_c/R_o	Λ (μm)	J_c (MJ/m^2)	K_c (MPa(m)$^{1/2}$)
Zr-1	4.88	0.0362	3.25	30	2	0.0217	48.64
Zr-2	4.54	0.0312	3.25	30	1.5	0.0136	38.53
Zr-2a	5.02	0.0312	3.25	30	1.5	0.0197	46.33
Zr-3	5.34	0.035	3.25	30	1	0.0187	45.20
Zr-8	5.62	0.029	3.25	10	0.5	0.00753	28.66
Zr-9	5.47	0.029	3.25	10	0.6	0.00809	29.72
Zr-10	4.98	0.0366	3.25	10	0.9	0.00651	26.66

orientation in alpha-annealed material. Although there is a rising *K*-resistance curve behavior observed in the LT and TL orientation for alpha-annealed Zircaloy-4, the process of unstable crack extension by void nucleation and growth at higher *K* values also is consistent with the predictions of this model.

6. Crack growth mechanisms, failure criteria, and texture

The current investigation has identified three mechanisms for quasi-static crack growth in alpha-annealed and beta-treated Zircaloy-4 that are illustrated in Figs. 23–25. The mechanisms for crack growth are described and discussed in terms of the results and failure criteria.

6.1. Crack growth mechanisms

Fig. 23 illustrates the process of crack tip blunting by emitting dislocations from the crack tip to form a slip band from a rounded tip, decohesion along and opening of the slip band into sharp, V-shaped vertices along the crack front, and subsequent crack opening by shearing and tearing along the original slip band or additional slip bands emitted from the V-shaped crack vertices. One or more vertices can form and advance the crack tip at various fronts. This crack growth mechanism has been observed in alpha-annealed Zircaloy-4 typically at *K* levels in the rising part of the *K*-resistance curve for LT and TL between K_c and the onset of unstable crack growth at *K* values of about 50 MPa $\sqrt{m}$.

The second crack growth mechanism shown in Fig. 24 involves the nucleation, growth, and coalescence of voids at small particles located ahead of the crack tip. This crack growth mechanism has been observed in both alpha-annealed and beta-treated Zircaloy-4, and leads to the presence of one or more coalesced voids at the crack tip, instead of local vertices along the crack front. This crack growth mechanism generally leads to unstable crack propagation. This crack growth mechanism generally occurs in alpha-annealed at *K* levels above 50 MPa $\sqrt{m}$ where unstable crack growth occurs, but is the predominant fracture mechanism in beta-treated where unstable crack propagation occurs in all orientations.

Fig. 25 illustrates the crack growth mechanism involving the emission of dislocations from the crack tip to form a slip band from the crack front and the formation of a void at the tip of the slip band. Decohesion along the slip band at the crack tip can result in crack extension. Furthermore, the slip band can also decohere at a segment further ahead of the crack to become a void that grows and links with other voids formed within the slip band. Thus, the third crack growth mechanism can be considered to be the cumulative processes of the first and the second fracture mechanisms that are operating either concurrently or one after the other. Furthermore, various sizes and shapes of dimples were observed on the fracture surfaces for both alpha-annealed and beta-treated Zircaloy-4, and tearing ridges are typically covered with voids or dimples. Thus, all three crack growth mechanisms are likely operative to some extent along the crack front and throughout the process zone at both the surface and through thickness direction. However, the model developed in the previous section only addresses the second process of void nucleation, growth, and coalescence.

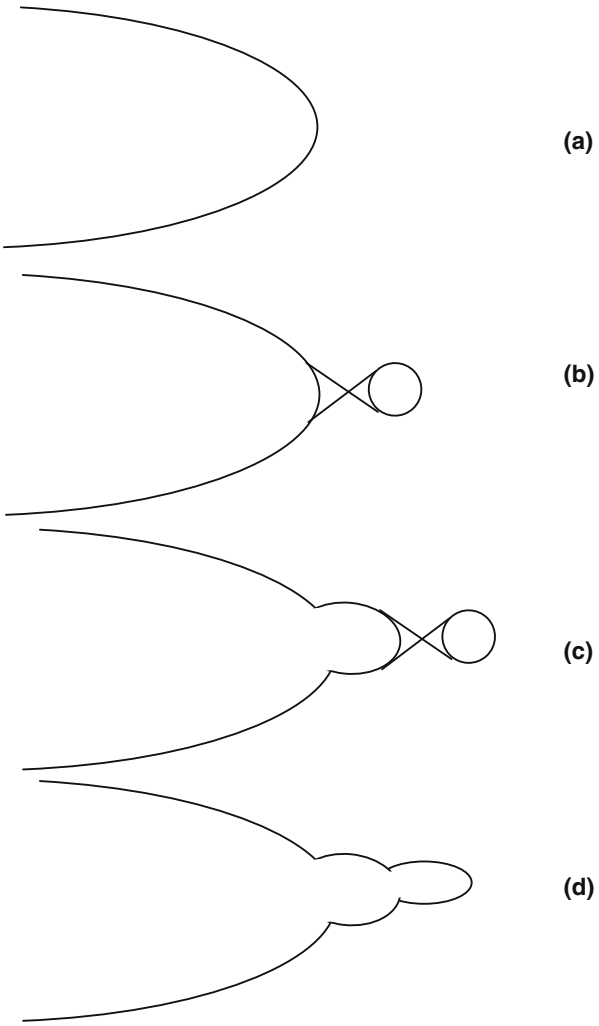

Fig. 24. Crack growth by void nucleation, growth, and coalescence: (a) blunt crack tip, (b) void formation ahead of blunt crack tip and shearing along slip lines in the ligament, (c) void links with crack tip to form a blunt crack tip; void nucleation repeats ahead of the blunt crack tip, and (d) crack tip with two coalesced voids.

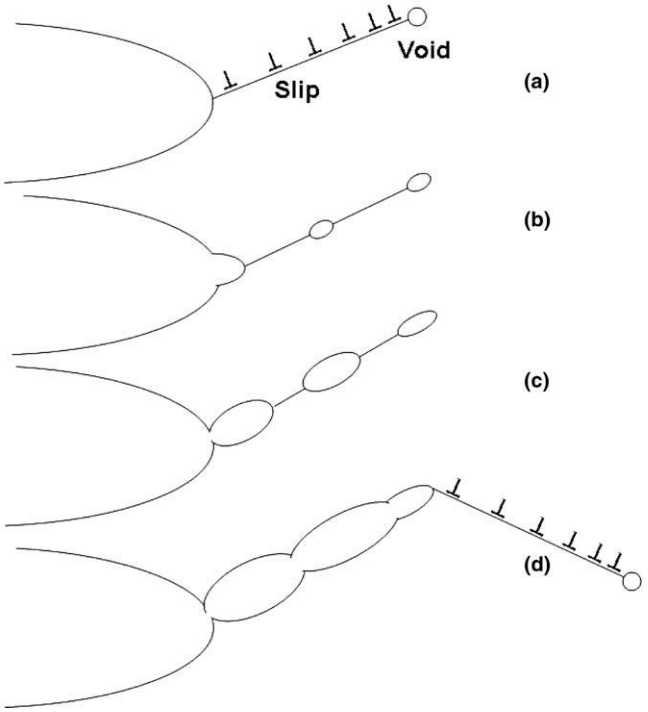

Fig. 25. Crack growth by a combination of dislocation emission from the crack tip to produce a slip band, slip band cracking, and void nucleation, growth, and coalescence: (a) dislocations emitted from the crack tip to produce a slip line emitted from a blunt crack tip with a void formed at the one end of slip line, (b) decohesion of slip line at the crack tip forms a vertex at the crack front and a small void along the slip line, (c) crack or void growth at multiple sites along the slip line, and (d) voids coalesce with crack tip and slip emission from the extended crack tip.

6.2. Failure criteria and model comparisons

Experimental observations and the micromechanical model indicate void growth and coalescence is the mechanism that results in the unstable crack extension observed for all orientations for both alpha-annealed and beta-treated Zircaloy-4. A critical strain criteria must be reached before void nucleation, growth and coalescence is initiated to produce the unstable crack extension. The critical strain criterion appears to be valid for also describing the onset of small quasi-stable tearing along slip bands. Such limited quasi-stable tearing along slip bands without any void nucleation, growth, and coalescence was observed in some cases at the onset of crack growth. However, tearing ridges on the fracture surfaces often show the presence of small voids aligned along the ridges and voids generally covered the majority of the fracture surfaces for both alpha-annealed and beta-treated materials. These observations suggest a critical strain criterion may be applicable to fracture mechanisms involving limited quasi-stable shearing along slip bands even though voids are not created. It is possible that the voids are created late in the tearing process as the tearing extends to larger lengths, and void nucleation, growth, and coalescence may occur at the point of unstable crack extension where the void formation occurs too quickly to be detected visually via SEM. On this basis, the critical strain criterion may be considered to govern the: (1) tearing along slip bands, (2) the nucleation, growth, and coalescence of voids with the crack tip, and (3) a combination of tearing along slip bands with and without void nucleation, growth, and coalescence.

6.3. Role of texture

The role of texture may be interpreted in terms of the type of grain boundaries and grain orientations present in alpha-annealed and beta-treated Zircaloy-4. Both LT and TL alpha-annealed samples produce a rising resistance curve behavior with higher steady-state fracture toughness K_{SS} values compared to beta-treated samples in all orientations. Beta-treated material shows the absence of a resistance curve behavior with lower K_c values in all orientations. The absence of resistance curve behavior also is observed for alpha-annealed material in the SL orientation, but the steady-state fracture toughness K_{SS} value is only slightly lower than values for LT and TL alpha-annealed Zircaloy-4 samples. The crystallographic texture in alpha-annealed material is conducive to slip on prism planes in samples with the LT and TL orientation. The occurrence of slip at lower stress likely allows more homogeneous deformation along slip bands so that void nucleation is avoided and a rising resistance curve behavior is observed. The SL orientation is in an unfavorable orientation for $\langle 11\bar{2}0\rangle$ slip on $\{10\bar{1}0\}$ prism planes so that slip requires higher stress levels. That is consistent with extensive void nucleation and growth that can lead to the observations of unstable crack extension.

The difference in toughness and fracture behavior between alpha-annealed and beta-treated Zircaloy-4 can be attributed to inherent differences in grain structure, texture, and distribution of Laves phase particles. The alpha-annealed microstructure exhibits a textured equiaxed grain structure with Laves phase particles distributed both within grains and at grain boundaries. The uniform distribution of precipitates results from the fact that all processing is performed in the temperature range where the alpha structure is stable and may be influenced by a fairly uniform distribution of grain boundary misorientation angles, as shown in Fig. 1. Beta-treated Zircaloy-4 is cycled into the temperature range where the beta phase is stable and the Laves phases dissolve so the iron and chromium go into solid solution. The alpha phase is formed upon cooling to room-temperature, the iron and chromium are less soluble in alpha so that the solute is rejected in both directions perpendicular to the lath axis. The iron and chromium solute segregates to the lath boundaries as the basket-weave structure of alpha laths is formed, and the Laves phases then nucleate at the lath boundaries. As a result, the Laves phase particles at the lath boundaries, which are small and closely spaced, are prone to dimpled fracture by void nucleation, growth, and coalescence in beta-treated Zircaloy-4. The crack growth in beta-treated Zircaloy-4 follows a fracture path that is predominantly along lath boundaries at lower K values by unstable crack extension. Once the crack extension commences, the closely spaced voids coalesce with the crack tip in succession with relative ease to result in unstable crack extension with no resistance curve fracture behavior. The more random distribution of Laves phase particles, both at grain boundaries and within grains, for alpha-annealed Zircaloy-4 results in higher toughness, and allows resistance curve behavior to develop in the LT and TL orientations where slip may occur at lower stress-levels. The discontinuity in texture at each colony boundary, and some of the lath boundaries, for beta-treated may also result in the build up of higher stresses at lath boundaries. Thus, texture appears to influence the fracture resistance of the zirconium alloy by controlling not only the slip behavior, but also the grain boundary precipitation and void formation processes.

7. Summary

In situ testing, OIM measurements of texture, fractography, and metallography were used to show that a mechanism of void coalescence controlled the deformation and fracture of Zircaloy-4. Rising R-curve behavior was observed for alpha-annealed Zircaloy-4 in the L–T and T–L orientations, with the initiation of crack extension at K values of 36–40 MPa $\sqrt{m}$ and increasing to K values of 58–62 MPa $\sqrt{m}$. Unstable crack extension was observed in the S–L orientation for alpha-annealed starting at a K value of 57 MPa $\sqrt{m}$. Unstable crack extension was observed in all orientations for beta-treated starting at K values of 35–39 MPa $\sqrt{m}$ with little or no rising in the K-resistance curve to maximum K values of 39–41 MPa $\sqrt{m}$. Unstable crack extension results from void growth and coalescence from Laves phase particles present within grains and at grain boundaries for alpha-annealed Zircaloy-4, and from the Laves phase particles at lath boundaries for beta-treated Zircaloy-4. This is a ductile fracture process as crack extension occurs by the tearing of the ligaments between the voids.

The texture in the LT and TL orientations for alpha-annealed Zircaloy-4 are conducive to slip on prism planes at low stresses, leading to stable crack extension along slip bands that result in the rising R-curve behavior. The texture in the SL orientation for alpha-annealed Zircaloy-4 is not aligned for slip on the prism plans so that higher stresses are need to produce slip band formation, but these high stresses result in unstable crack propagation by void growth and coalescence. All lath boundaries in beta-treated Zircaloy-4 are covered with Laves phase particles. Void nucleation and growth from the Laves particles results in unstable crack extension along the lath boundaries for beta-treated Zircaloy-4 at lower K values than for alpha-annealed. The discontinuity in texture between the lath grains may also increase stresses at the lath boundaries to accelerate the void growth process observed for beta-treated Zircaloy-4. A micromechanical model is developed that predicts the observed R-curve fracture resistance based on a void nucleation, growth, and coalescence mechanism.

Acknowledgements

This work was supported under USDOE Contract No. DE-AC11-98PN38206. The advice and review from R.W. Smith and J.E. Hack

is appreciated. The technical assistance by J.L. Martinez in performing the in situ fracture testing and metallography and by M. Juarez in performing the fatigue pre-cracking and tensile testing, and EBSD Analytical for the OIM is acknowledged.

References

[1] R.A. Holt, J. Nucl. Mater. 35 (1970) 322.
[2] O.T. Woo, K. Tangri, J. Nucl. Mater. 79 (1979) 82.
[3] O.T. Woo, D.T. Seng, K. Tangri, S.R. MacEwen, J. Nucl. Mater. 87 (1979) 135.
[4] P.H. Kreyns, W.F. Bourgeois, C.J. White, P.L. Carpentier, B.F. Kammenzind, D.G. Franklin, in: E.R. Baradley, G.P. Sabol (Eds.), Zirconium in the Nuclear Industry: Eleventh International Symposium, ASTM STP 1295, American Society for Testing and Materials, 1996, pp. 758–782.
[5] D. Churquet, R. Haton, E. Ortlieb, J.-P. Gros, J.F. Wadier, in: L.F.P. Van Swam, C.M. Euken (Eds.), Zirconium in the Nuclear Industry: Eighth Symposium, ASTM STP 1023, ASTM Philadelphia, PA, 1988, pp. 405–422.
[6] C. Lemaignan, A.T. Motta, in: R.W. Cahn, P. Haasen, E.J. Kramer, (Eds.), Zirconium Alloys in Nuclear Applications, Nuclear Materials, B.R.T. Frost (Ed.), vol. 10B, Materials Science and Technology, VCH, New York, 1994, pp. 1–51 (Chapter 7).
[7] D. Arias, T. Palacios, C. Turrillo, J. Nucl. Mater. 148 (1987) 227.
[8] G. Bertolino, G. Meyer, J.P. Ipiña, J. Nucl. Mater. 322 (2003) 57.
[9] A.H. Yawny, J.P. Ipiña, J. Test. Eval. 31 (2003) 413.
[10] M. Ahmad, J.I. Akhter, M.A. Shaikh, M. Iqbal, W. Ahmad, J. Mater. Eng. Perform. 12 (2003) 179.
[11] J.C. Rawers, W.D. McMullen, Eng. Fract. Mech. 13 (1980) 979.
[12] V. Grigoriev, B. Josefsson, J. Nucl. Mater. 257 (1998) 99.
[13] D. Lee, E.F. Koch, H.C. Rogers, Metall. Trans. 1 (1970) 3125.
[14] L. Xiao, Y. Umakoshi, J. Sun, Mater. Trans. A 32A (2001) 2841.
[15] T.M. Link, D.A. Koss, A.T. Motta, Mater. Trans. A 31A (2000) 1883.
[16] S.R. MacEwen, C.E. Ells, O.T. Woo, J. Nucl. Mater. 101 (1981) 336.
[17] J. Huang, C. Ho, Mater. Chem. Phys. 47 (1997) 184.
[18] L. Xiao, H. Gu, J. Eng. Mater. Technol. 120 (1998) 114.
[19] K.W. Lee, S.K. Kim, K.T. Kim, S.I. Hong, J. Nucl. Mater. 295 (2001) 21.
[20] T.J. Walker, J.N. Kass, Zirconium in the Nuclear Applications, ASTM STP 551, American Society for Testing and Materials, 1974, pp. 328–354.
[21] T.J. Walker, Nucl. Technol. 16 (1972) 509.
[22] L.A. Simpson, C.K. Chow, in: R.B. Adamson, L.F.P. van Swam (Eds.), Zirconium in the Nuclear Industry: Seventh International Symposium, ASTM STP 939, American Society for Testing and Materials, 1987, pp. 579–596.
[23] K.S. Chan, Metall. Trans. 27A (1996) 2518.
[24] B.V. Cockeram, K.S. Chan, Metall. Trans. 39A (2008) 2045.
[25] ASTM E812-97, ASTM, Philadelphia, PA, 1997.
[26] ASTM E813-95, ASTM, Philadelphia, PA, 1995.
[27] T.G.F. Gray, Int. J. Fract. 13 (1997) 65.
[28] J.J. Kearns, WAPD-TM-473, DOE/OSTI, Oak Ridge, TN, 1965.
[29] J.J. Kearns, J. Nucl. Mater. 299 (2001) 171.
[30] A. Nagy, J.B. Campbell, D.L. Davidson, Rev. Sci. Instrum. 55 (1984) 778.
[31] F.H. Huang, W.J. Mills, Nucl. Technol. 107 (1993) 367.
[32] F.H. Huang, J. Nucl. Mater. 207 (1993) 103.
[33] K.S. Chan, Metall. Mater. Trans. A 34A (2003) 43.
[34] H. Anton, P.C. Schmidt, Intermetallics 5 (1997) 449.
[35] A. Saxena, D.C. Daly, H.A. Ernst, K. Banerji, in: J.P. Gudas, J.A. Joyce, E.M. Hackett (Eds.), Fracture Mechanics: Twenty-First Symposium, ASTM STP 1074, ASTM, Philadelphia, 1990, pp. 378–395.
[36] J.W. Hutchinson, J. Mech. Phys. Solids 16 (1968) 13–31.
[37] J.R. Rice, G.F. Rosengren, J. Mech. Phys. Solids 16 (1968) 1.
[38] J.R. Rice, J. Appl. Mech. 35 (1968) 379.
[39] C.F. Shih, Tables of Hutchinson–Rice–Rosengren Singular Field Quantities, Materials Research Laboratory Report, MRL E-147, Brown University, Providence, RI, 1983.
[40] J.B. Rice, D.M. Tracey, J. Mech. Phys. Solids 217 (1969) 201.
[41] N. Aravas, R.M. McMeeking, J. Mech. Phys. Solids 33 (1985) 25.